U.PORTO

FEUP FACULDADE DE ENGENHARIA UNIVERSIDADE DO PORTO

Multi Scale Lumen Boundaries Segmentation and its 3D Representation

Jorge Miguel Silva Pereira

MSc Course in Biomedical Engineering

July 2012

FEUP FACULDADE DE ENGENHARIA
UNIVERSIDADE DO PORTO

Multi Scale Lumen Boundaries Segmentation and its 3D Representation

M.Sc. Thesis

Jorge Miguel Silva Pereira

Supervised by:

João Manuel R. S. Tavares

Associated Professor at the Mechanical Engineering Department

Faculty of Engineering of the University of Porto

Abstract

The carotid artery is extremely important on the blood supply to the head and neck zones. This importance is even greater, on the blood supply of the brain, as it is one of the most sensitive organs in the organism. The brain uses about 15% of the blood stream and consumes about 20% of oxygen and glucose from the organism, due to his huge demand in energy (ATP). It works based on a highly oxygenated metabolism and easily suffers perturbations, in the absence of this molecule. It takes only a simple gap of 10 seconds on the blood supply to the brain, to cause the loss of conscience and if this period was expanded for 4 minutes or more, it can result in severe and permanent harm to the brain.

Several situations may put in danger the healthiness of the brain's functions and structures. From a simple physical trauma to a physiological pathology, there are a range of harmful situations this organ. The atherosclerosis is one of the pathologies that affect its functions as it slowly reduces the blood supply on the artery. It characterized by a disposal of a hard substance on the carotid artery wall. Besides blocking the blood flux it also may unleash small segments that may compromise the artery structure causing a stroke. It is one of the main causes of brain damaging, becoming quickly one of the major causes of death in the occidental world, as it is catalyzed by a sedentary way of life and bad alimentation typical of this society.

The hemodynamic is one of the most promising tools for the atherosclerosis prevention. It studies the blood flux trough the arteries, notifying the changes that may occur or catalyze this kind of accidents. To work on this field it is required to have 3D models of the arteries in order to simulate some stress situations and to improve the parameters analyzes.

Under the scope of the present Thesis, a novel method was developed to provide a suitable 3D model base for the hemodynamic studies evolution. It begins by studying the proprieties of the B-mode carotid image, as it is one of the affordable, armless and one of the most widely used imaging systems in the world. The main objective of this study is to achieve the knowledge to develop

a method to segment the lumen boundaries of the carotid on ultrasound b-mode images. The lumen is the main target because it is within it that the blood flows. Executing the segmentation is a primer objective as it allows the posterior 3D representation. This is only possible based on the assumption that if a successful lumen boundaries detection is implemented, the diameter between the 2D lumen walls may be computed into a 3D circle representation of it. Having a 3D model of the 2D b-mode images, the rest it is up to the hemodynamic.

As said so, this work aims to segment the full lumen boundaries and create its 3D representation for modeling purposes.

Resumo

As artérias da carótida são de extrema importância, no fornecimento de sangue às zonas do pescoço e da cabeça. Esta importância é muito maior no fornecimento de sangue ao cérebro, já que se trata de um dos órgãos mais sensíveis do organismo. O cérebro recebe cerca de 15% da circulação sanguínea e consome cerca de 20% do oxigénio e glucose do organismo, devido à sua grande necessidade de energia sobre a forma de ATP (adenosina trifosfato). Ele trabalha baseado num metabolismo oxigenado e sofre facilmente perturbações, na ausência desta molécula. Um simples intervalo de 10 segundo sem fornecimento de sangue ao cérebro pode causar perda da consciência e se este período for expandido por 4minutos ou mais, pode resultar num dano irreversível no cérebro.

Várias situações podem pôr em perigo a estabilidade das funções cerebrais ou das suas estruturas. Desde um simples trauma físico a uma patologia fisiológica, existe um leque enorme de situações que são perigosas para este órgão. A aterosclerose é uma das patologias que afetam as suas funções, pois vai reduzindo lentamente o acesso do fluxo sanguíneo pela artéria. É caraterizada pela deposição de uma substância dura nas paredes da carótida. Para além de bloquear o fluxo do sangue, também pode soltar pedaços da placa que podem pôr em perigo a estrutura da artéria, provocando acidentes cerebrovasculares. Esta é uma das principais causas de danos no cérebro e uma das principais razões de morto no mundo ocidental, que tipicamente tem um estilo de vida sedentário e uma alimentação abusiva.

A hemodinâmica é uma das ferramentas mais promissoras para a prevenção desta patologia. Estudo o fluxo do sangue pelas artérias, verificando as mudanças que possam ocorrer que catalisem estes acidentes. Para trabalhar nesta área são necessários modelos3D da carótida para se poder simular situações de esforço da mesma e apurar a análise de dados.

Na presente Dissertação foi desenvolvido um novo método para a criação de uma base de modelo 3D para usar em estudos de hemodinâmica. Começou-se por fazer um amplo estudo das propriedades das imagens B-Mode de ultra-som da carótida, um dos sistemas de imagem mais baratos, inofensivos e usados do mundo. O objetivo do estudo foi recolher conhecimento suficiente para potencializar a criação de um método de segmentação dos limites do lúmen da carótida neste tipo de imagens.

O lúmen é de facto o principal alvo neste trabalho, porque é nele que ocorre o fluxo do sangue. Executando com sucesso uma segmentação destas paredes é uma grande necessidade, pois permite partir para a sua representação 3D. Isto apenas é possível baseado no pressuposto de que o diâmetro entre as paredes segmentadas, podem ser computadas para uma representação 3D circular dessa posição. Tendo então a representação 3D da imagem do ultra-som2D, o resto do trabalho parte para a hemodinâmica.

Em suma o objetivo desta dissertação foi segmentar completamente as paredes do lúmen e criar a sua representação 3D para fins de modelação.

Contents

Acknowledgements

The author would like to thanks:

Prof. João Manuel R S Tavares for the supervision given trough the development of this Thesis.

My family and friends for supporting me all the time along my studies and for being proud on my academic path.

Diana Santos, student at the Faculty of Engineering of the University of Porto, for all the aid given and support during the writing of the Thesis.

Raquel Parreira, student of Medicine at the Faculty of Medicine of the University of Lisbon, which provided their cardiovascular notes.

Nilza Ramião, student at the Faculty of Engineering of the University of Porto, which provided their anatomical Books and her aid.

List of figure s

List of tables

List of Abbreviations

ATP - *Adenosine* triphosphate

CCA- Common carotid artery

CPR - cardiopulmonary resuscitation

ECG - Electrocardiogram

Eq. - Equation

fig. - Figure

FOAM- first-order absolute moment edge detector

IMT- Intima–media thickness

ms^{-1}- Meters per second

MSE- Mean square error

Chapter I - Introduction

Chapter I – Introduction

1.1 Motivation

The carotid artery is extremely important on the blood supply to the head and neck zones. This importance is even greater, on the blood supply of the brain, as it is one of the most sensitive organs in the organism. The brain uses about 15% of the blood stream and consumes about 20% of oxygen and glucose from the organism, due to his huge demand in energy (ATP). It works based on an highly oxygenated metabolism and easily suffers perturbations, in the absence of this molecule. It takes only a simple gap of 10 seconds on the blood supply to the brain, to cause the loss of conscience and if this period was expanded for 4 minutes or more, it can result in severe and permanent harm to the brain [SEELEY, 2004], [MOORE, 2006].

The atherosclerosis is one of the pathologies that affect its functions as it slowly reduces the blood supply on the artery. It is one of the principle causes of cerebrovascular accidents, becoming quickly one of the major causes of death in the occidental world.

As it is a pathology highly associated to the zone where blood flux is disturbed, the hemodynamic and medical imaging has been studying several ways to detect and understand its process. One larger field of study in this thematic is focused on B-mode carotid imaging, as it is one of the affordable, armless and one of the most widely used image systems the world. In order to improve the studies on this area, 3D models of the lumen of the carotid artery are necessary, and it is based on this that this Thesis was carried out. As the 3D model is full computed, it can easily move the next step of conversion to finite elements and its fluid velocity study.

1.2 Aims

The aim of this Thesis is to develop a novel method of carotid lumen ultrasound segmentation and building up its 3D representation, so in future it can be used as a base of 3D finite element models to be used in hemodynamic studies on atherosclerosis.

1.3 Structure

The present Thesis organized into seven chapters. In the next chapter there will be an introduction to the anatomy of the heart and the carotid artery, in order to introduce fundamentals concepts. This chapter is followed by another one where the ultrasound is fully explored and introduced other important technical concepts. In the fourth chapter there will be a review of the state of the art, within the segmentation of the carotid artery in B-mode images.

Afterwards, there is the full and detailed explanation of the novel multi-scale method developed, followed by a chapter of results and discussion.

In the end there will a conclusion where all the work will be commented, and some future tasks proposed.

Chapter II – Anatomy of the heart and the carotid artery

Chapter II – Anatomy of the heart and the carotid artery

2.1 Introduction

In this chapter is presented the study of the carotid anatomy since is foundations, following blood circulation logic, which is the reason that this chapter begins with the description of the heart is anatomies.

Firstly, a fully description of the hearts anatomy is realized, developing all the process realized until it reaches the carotid artery. When that happens, it will be focused on describing his own anatomy and principles.

2.2 Shape and Location of the Heart

The location and shape of the heart it is an important issue in the medical area. This knowledge improves the efficacy of certain clinical acts like positioning the stethoscope, performing an ECG or CPR [SEELEY, 2004].

With an approximated size of a closed fist, and a shape like a blunt cone, the heart is located in the mediastinum (figure 1) of the thoracic cavity. This is the midline partition, of this cavity, which also includes other structures like trachea or esophagus [SEELEY, 2004].

In a normal thoracic cavity, the heart stands obliquely in the mediastinum (figure 1). Its base (located from behind the sternum to the second intercostals space) is directed posteriorly and slightly superiorly to the right and its apex (approximately 9cm to the left of the midline of the sternum) is directed anteriorly and inferiorly to the left. Due to this disposition, the majority of the heart is mass is located to the left of the midline of the sternum [SEELEY, 2004].

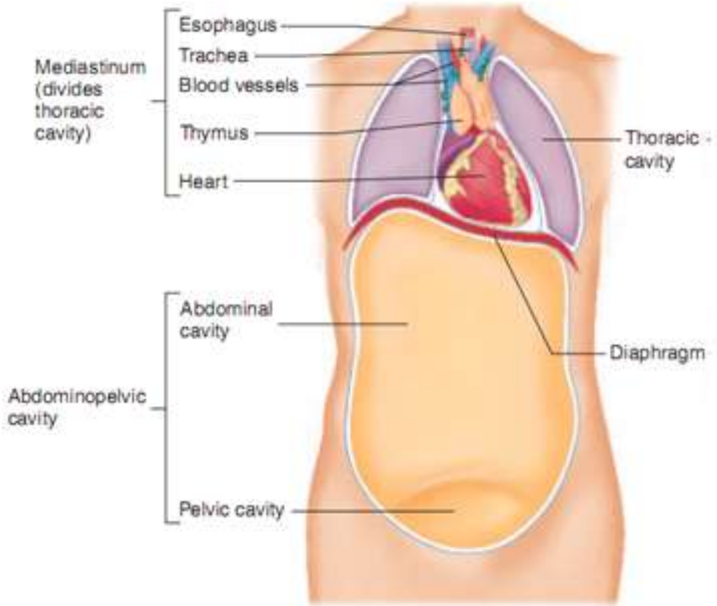

Figure 1– Thoracic cavity (adapted from [SEELEY, 2004])

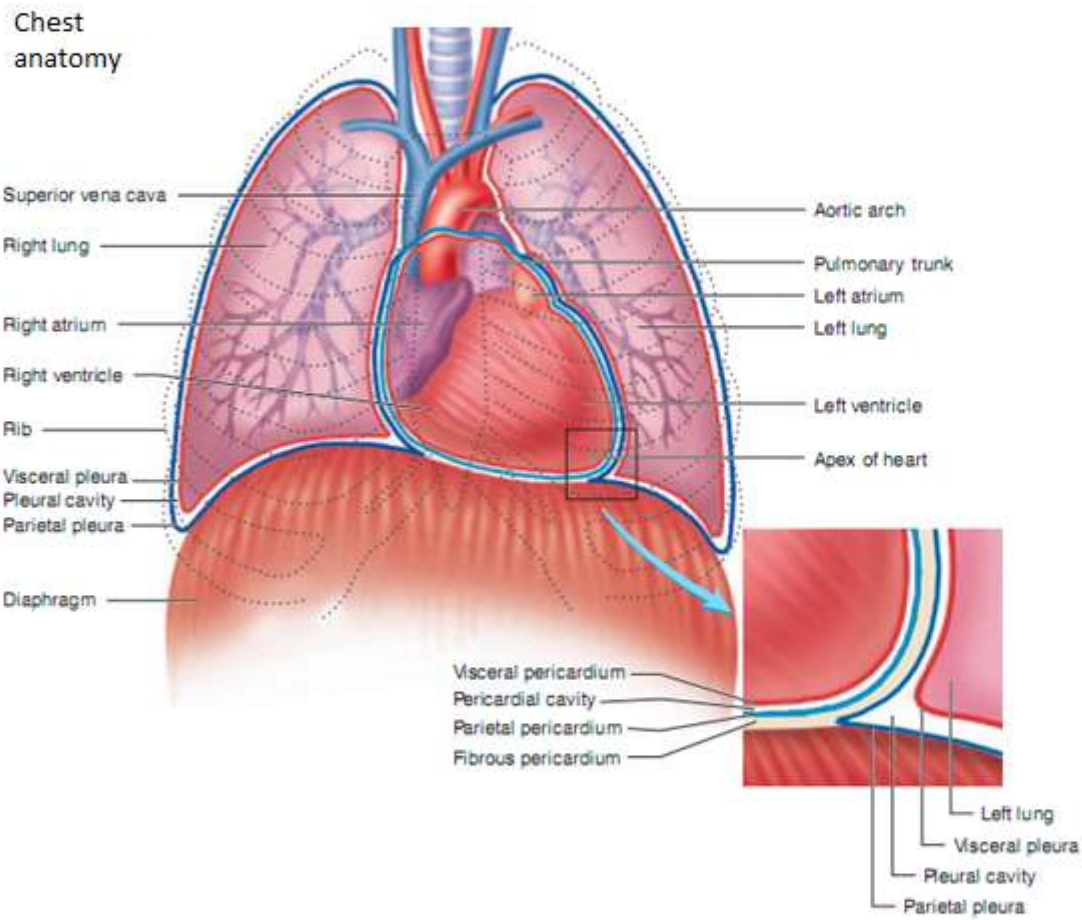

Figure 2 – Location of the heart (adapted from [SEELEY, 2004])

2.3 Functions of the Heart

- Creating blood pressure through heart is contractions.
- Routing blood, by separating pulmonary and systemic circulations and providing better tissue oxygenation.
- Getting a one-way blood flow, using cardiac valves.
- Controlling blood supply. Alter frequency and force of heart contractions, according to metabolic needs of the tissues.

2.4 Heart and blood flow

The heart is mainly composed by four different chambers surrounded by a double-layered closed bag, the pericardium. These chambers are divided into two atria and two ventricles. The superior and posterior portions of the heart belong to the thin-walled atria and the anterior and inferior portions to the thick-walled ventricles. The atria receive the blood from the several circulations, and the ventricles pump it out [SEELEY, 2004].

The two atria are separated from each other by the interatrial septum. The right atrium is the receptor of the systemic circulation. It receives the blood, from the body, trough the two openings of the inferior and superior vena cava. This chamber has also another major opening that belongs to the coronary sinus, which allows the heart to receive the blood from the coronary circulation (blood from the heart itself). The left atrium is in charge of the reception of the pulmonary circulation, which receives the blood, across the four pulmonary veins, from the lungs [SEELEY, 2004].

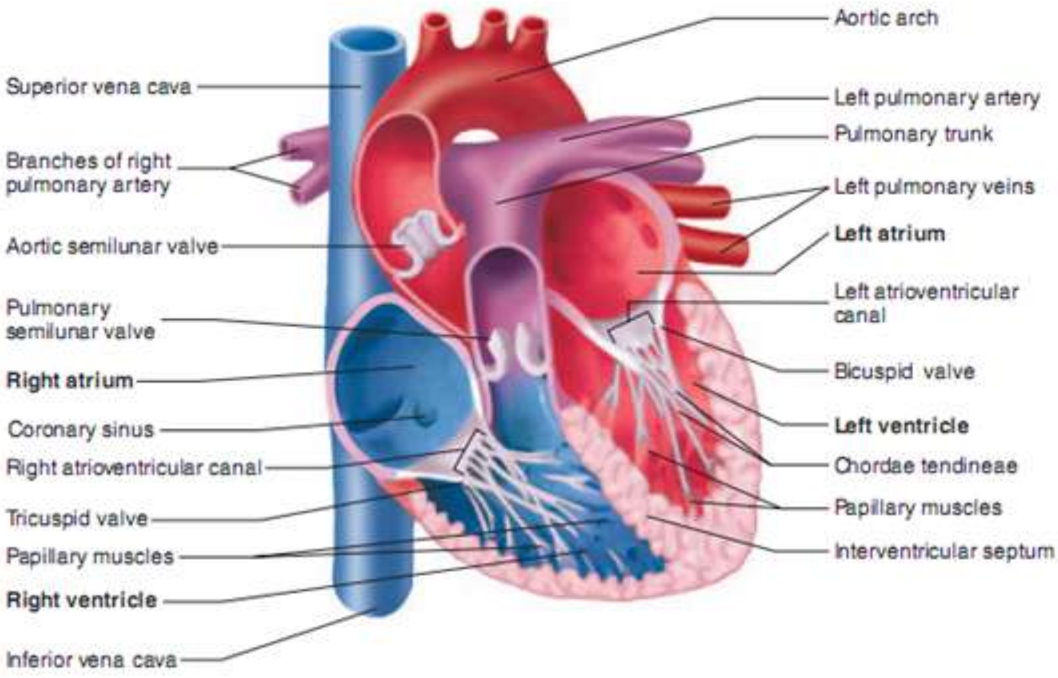

Figure 3 – Anatomy of the heart (adapted from [SEELEY, 2004])

The atria opens into two ventricles, which are separated from each other by the interventricular septum. The blood flow, from the atria trough the ventricles, is controlled by the atrioventricular valves. These valves allow blood to flow only from the atria into the ventricles, preventing a backwards reflux. Between the right atrium and the right ventricle, there is a valve composed by three cusps, therefore called the tricuspid, contrasting with the two cusps valve, between the left atrium and left ventricle, called bicuspid. Attached to the cusps, by a thin and strong connective tissue named chordate tendineae, are the cone-shaped papillary muscles. This muscles contract when the ventricles contract, preventing the atrioventricular valves from opening, by pulling the chordate tendineae [SEELEY, 2004].

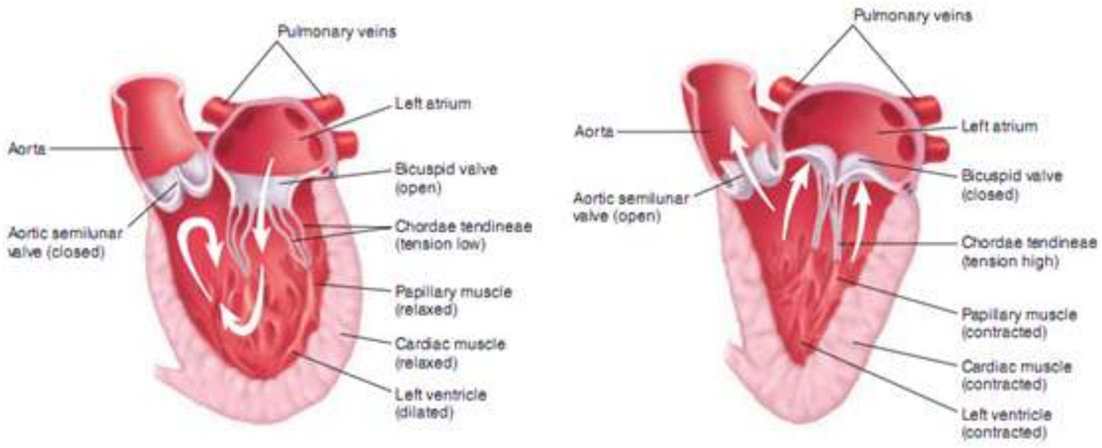

Figure 4– Valves of the heart (adapted from [SEELEY, 2004])

Superiorly placed in each ventricle is a large outflow route of the blood. The right ventricle opens into the pulmonary trunk, and the left into the aorta. The semilunar valves, which consist in a three pocketlike semilunar cusps, are responsible for the control of the blood route flow from the ventricles to the aorta and pulmonary trunk. If for some reason the blood flows back from the blood vessels to the ventricles, It enters in the pocket of the cusps, making the cusps to meet and consequently, closing the semilunar valves [SEELEY, 2004].

2.5 Carotid artery

The carotids are extremely important arteries on the blood supply of the neck and head portions of the body. This importance is much higher on the blood supply of the brain as it is one of the most sensible organs of the organism. The brain receives 15% of blood circulation and consumes 20% of the body is oxygen and glucose due to is high demand for ATP. It works based on oxidative metabolism and quickly malfunctions in the absence of oxygen. A simple 10 second interruption of the blood supply can cause loss of consciousness and if we extend this interruption for 4 minutes or more, it can cause irreversible brain damage [SEELEY, 2004].

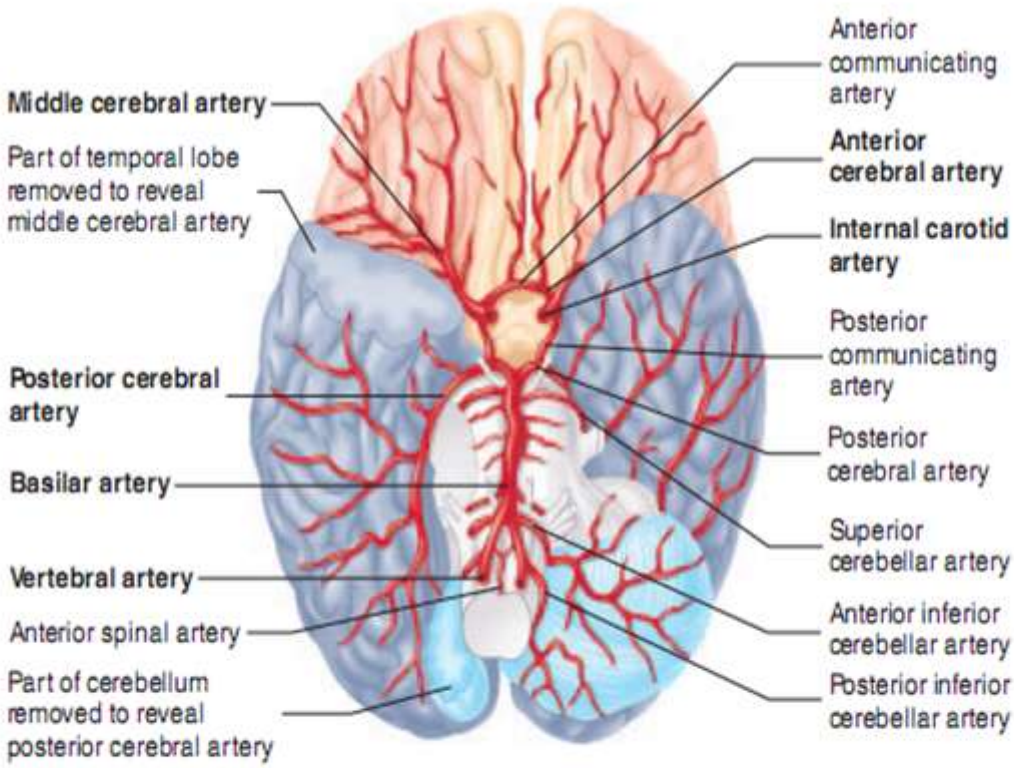

Figure 5 – Carotid ramifications on the brain (adapted from [SEELEY, 2004])

The arteriosclerosis is one of the pathologies that affect this function, as it slowly reduces blood flow through the carotid arteries [SEELEY, 2004].

The carotid are divided into right common carotid and left common carotid [SEELEY, 2004].

From the first branch of the aortic arch comes the brachiocephalic artery, which is a very short artery and forms the right common carotid and the subclavian artery. The first one transports the blood to the right side of the head and neck and the second to the right upper limb [SEELEY, 2004].

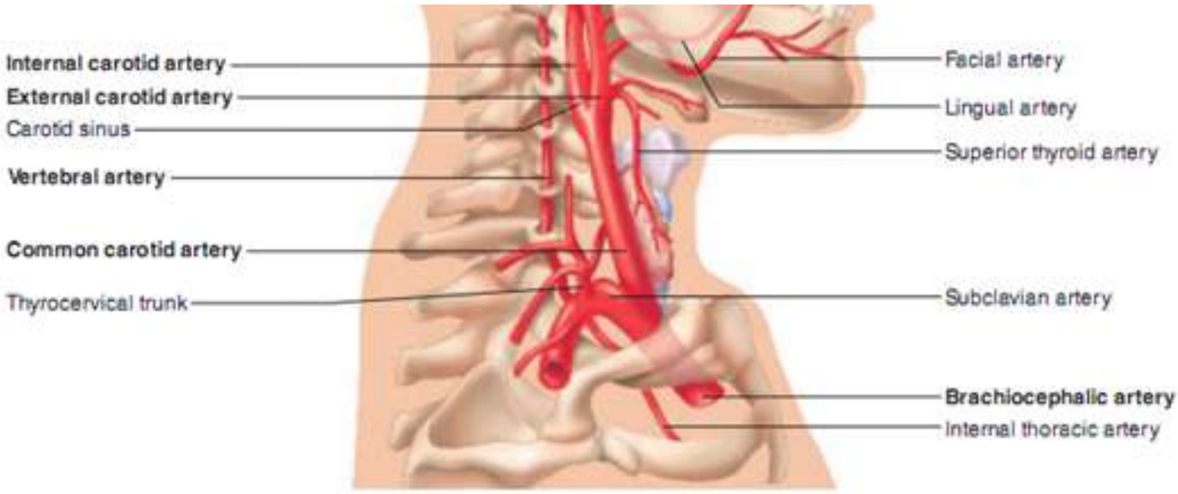

Figure 6 – Right common carotid artery (adapted from [SEELEY, 2004])

From the second branch of the aortic arch comes directly the left common carotid, which supplies blood to the left side of the head and neck [SEELEY, 2004].

The common carotid arteries extend superiorly along both sides of the neck until reach the inferior angle of the mandible, where each one branches into internal and external carotid arteries. In the beginning of this bifurcation on the internal carotid branch, the artery is slightly dilated to form the carotid sinus, which is important in monitoring blood pressure due to the baroreceptor reflex [SEELEY, 2004].

These baroreceptors, located also on the aorta, are pressure sensors that send continual information to the cardiac center. If the blood pressure drops, the cardiac center is informed and increases the heart rate, raising then the blood pressure. If the blood pressure is too high, the inverse response will happen, and the cardiac center reduces the heart rate [SEELEY, 2004].

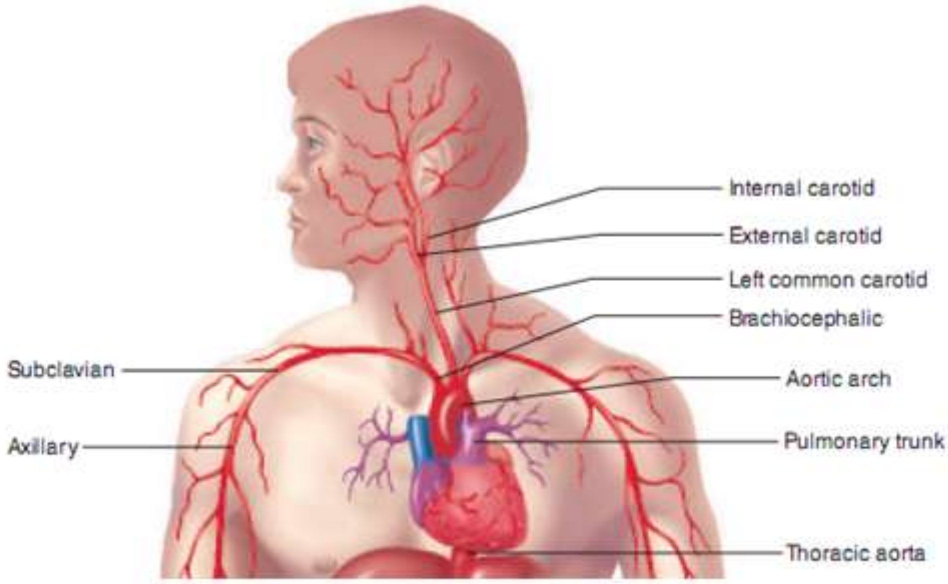

Figure 7– Left common carotid artery (adapted from [SEELEY, 2004])

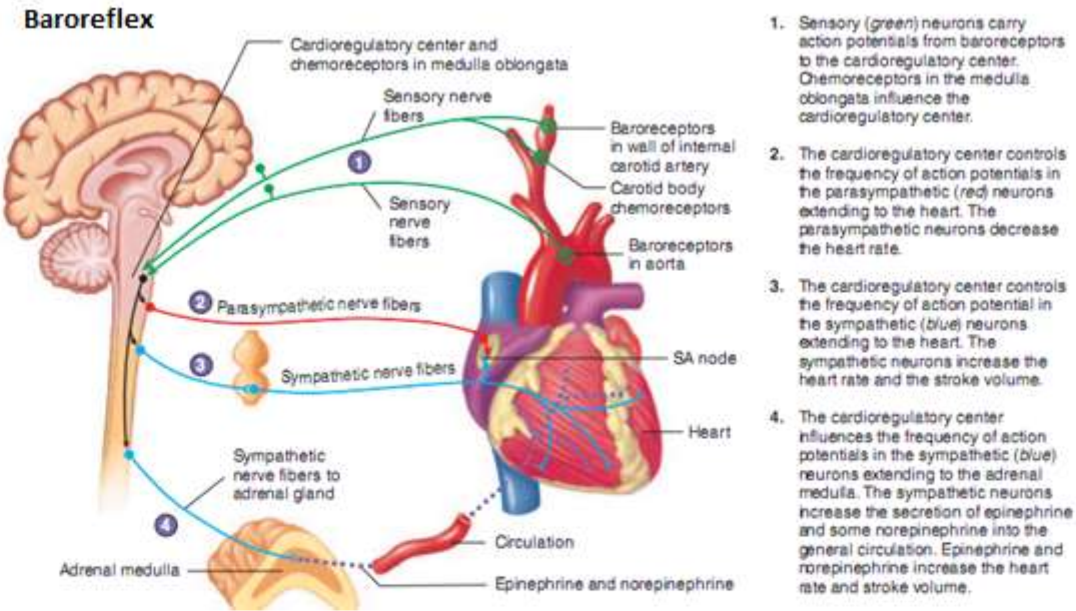

Figure 8 – Baroreflex system (adapted from [SEELEY, 2004])

The internal carotid arteries, which enter the cranial cavity through the carotid canal of the temporal bone, supply the orbits and about 80% of the cerebrum. From the cranial cavity the internal carotid gives rise to different branches (table 1). The external carotid arteries with their several branches along the external side of the cranium, supplies the neck and most external head structures (table 1).

Arteries	Tissues Supplied
External Carotid	
Superior thyroid	Neck, larynx and thyroid gland
Lingual	Tongue, mouth, and submandibular and sublingual glands
Facial	Mouth, pharynx and face
Occipital	Posterior head and neck and meninges around posterior brain
Posterior auricular	Middle and inner ear, head and neck
Ascending pharyngeal	Deep neck muscles, middle ear, pharynx, soft palate, and meninges around posterior brain
Superficial temporal	Temple, face and anterior ear
Maxillary	Middle and inner ears, meninges, lower jaw and teeth, upper jaw and teeth, temple, external eye structures, face, palate and nose
Internal Carotid	
Posterior communicating	Joins the posterior cerebral artery
Anterior cerebral	Anterior portions of the cerebrum and forms the anterior communicating arteries
Middle cerebral	Most of the lateral surface of the cerebrum
Ophthalmic	To the orbits, nose and forehead

Table 1– Brunches of the carotid artery in the brain (adapted from [SEELEY, 2004])

2.6 Atherosclerosis in the carotid

Atherosclerosis is an inflammatory chronic disease of blood vessels caused by the accumulation of fatty materials in artery walls, known as atheromatous plaque.

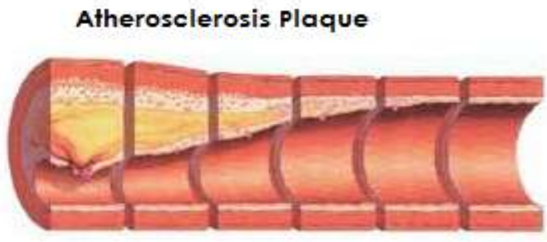

Figure 9 – Atherosclerosis (adapted from [NETTER, 2002])

This plaque causes the thickening (stenosis) of the artery reducing the blood flow through it and the blood supply to the target tissues. In extreme cases, the stenosis can be so severe, that the lumen is highly obstructed and the blood supply to the downstream tissues is insufficient, resulting in ischemia. Also the rupture of the fibrous cap, surrounding the plaque, exposes thrombogenic material to the circulation and can induce thrombus formation in the lumen. This thrombus travels into the blood stream, resulting in a quickly slowing or stopping of the blood flow. This vascular event is generally called an infarction, and in this case of study is known as cerebrovascular accident, resulting in a loss of brain functions[NETTER, 2002].

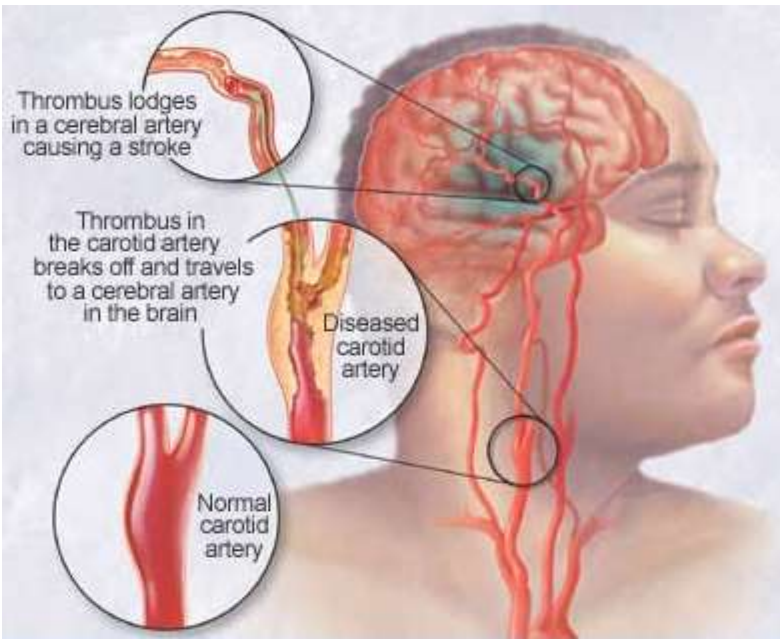

Figure 10– Thrombus causing a stroke (adapted from [NETTER, 2002])

2.7 Resume

This chapter reviewed the anatomy, structure of the carotid artery, from the beginning of its flux cycle to the end. This cycle begins at the heart, which is located on the chest area between the lungs. One of his functions is to input pressure to the blood so it can flow normally into the rest of the body. One of the targets of that blood flux is the carotid artery.

The carotid is one of the most important arteries on the human system as it supplies the head and neck zones through its ramifications.

The blood flux comes from the heart trough, along with the brain one of the most important organs in the body, the aortic arch into the carotid artery. This blood flux is then headed to several brunches into the several zones, as the brain.

Any malfunction on this cycle may lead to severe damage on the brain, as it is a highly oxygenic organ. One of the most common pathology on the carotid artery is the atherosclerosis, which is characterized by a deposition of one hard substance on the carotid wall, creating a dangerous plaque that slows down the flux. Besides the interference with the flux, this plaque may unleash parts of it that can travel through the blood and create an injury on the artery. This situation may cause a cerebrovascular accident and permanently damage the brain.

Chapter III – Ultrasound Imaging System

Chapter III –Ultrasound Imaging System

3.1 Introduction

In this chapter is introduced the ultrasound imaging system, explaining its basic principles, processes and image modalities.

This chapter will follow a generic to specific logic, where it starts by describing the basic principles of an ultrasound system, and then develops to their specific cases and to the image modalities, specially the B-mode.

3.2 Principles

The ultrasound imaging uses high-frequency (1-10MHz) sound waves and their echoes to produce images that can demonstrate the organ movement in real time. Using non-ionizing waves, unlike other imaging methods based on electromagnetic waves (x-ray, γ-ray…), the ultrasound becomes a quite frequent and safe choice in clinical practice, despite the noise inherent in this technique [DOUGHERTY 2009], [GONZALEZ 2001], [RUSS 2007].Usually an ultrasound system works with 1 to 5 pulses per microsecond, generated by an ultrasound transducer that contains a piezoelectric crystal surrounded by a pair of electrodes. When a small sinusoidal voltage is applied to the crystal, a resonance phenomenon occurs, producing then sound waves [DOUGHERTY 2009].

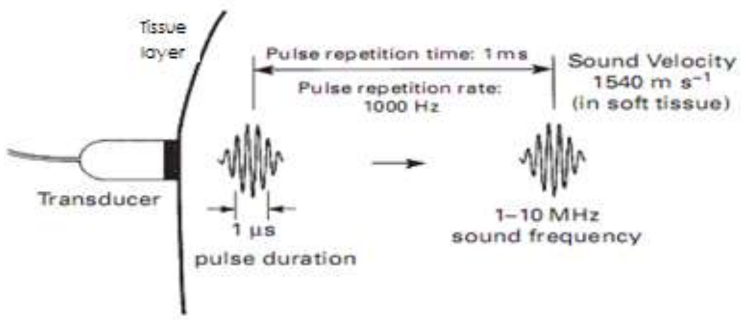

Figure 11– Schematic clinical ultrasound beam (adapted from [DOUGHERTY 2009])

A clinical ultrasound system is based on a basic procedure. The ultrasound probe (transducer inside) produces high frequency sound waves to the body. These waves will travel into the body and when they hit a boundary between tissues, a fraction of the wave is backscattered back to the probe, according to the different acoustic properties of the tissues. Generally, a gel is applied to the sky to minimize the present of air between the probe and the skin, in order to avoid reflection in that surface [DOUGHERTY 2009], [GONZALEZ 2001], [RANGAYYAN 2005].

The speed of the sound, v, in a certain material depends directly of its density, ρ, and its compressibility, K, according to:

$$v = \frac{1}{\sqrt{K\rho}} \tag{3.1}$$

We can see this dependence from the comparison of bone with soft tissue. Although bone has a higher density, it has a much smaller compressibility than soft tissue. So the product from $K\rho$ is higher for soft tissue than bone, resulting in a higher velocity for sound waves through the bone [DOUGHERTY 2009].

As the sound waves are longitudinal, only backward and forward movement in the same direction that the wave is travelling are induced on the particles of the tissues. Due to this behavior, generally, only those waves that reflect about 180° can contribute to the construction of the ultrasound image. This construction is achieved by measuring the delay between the pulse transmission and pulse reception on the probe, after a boundary reflection. Knowing also the speed of propagation of the beam, the depth of the several features from the target can be calculated and observed [DOUGHERTY 2009], [GONZALEZ 2001].

Despite all the different materials and tissues, we have in our body the ultrasound systems usually use the standard velocity for sound waves propagation trough soft tissue (1540 ms^{-1}), as the value for the previous data calculation[DOUGHERTY 2009], [GONZALEZ 2001].

Intensity of the echo is used to determine the brightness of the image, at the reflecting tissue surface. The intensity reflection coefficient, R, is given as:

$$R = \frac{(Z_1 - Z_2)^2}{(Z_1 + Z_2)^2} \tag{3.2}$$

Where Z_1 andZ_2, are the acoustic impedance of each surface is material side. The acoustic impedance is constant for a specific material (table 2), and is given by:

$$Z = \rho v = \sqrt{\frac{\rho}{k}} \tag{4.3}$$

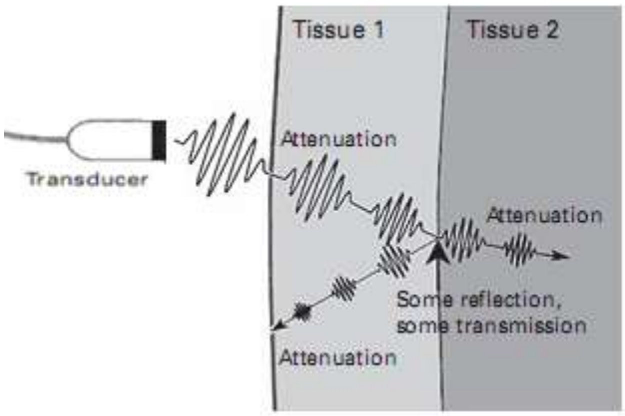

Figure 12 –Attenuation and reflection of the echo pulse (adapted from [DOUGHERTY, 2009])

If the materials are very acoustically similar, there is little reflection; however, if there is a large difference between them, a lot of reflections will happen. For example, the bone and soft tissue, their acoustic miss-match creates a strong echo with about 40% of the incident intensity. This reflection can achieve to 99% if, for example, the two materials are soft tissue and some kind of gas. This heavy attenuation, along with the decrement of the intensity with propagation distance, leads to a very difficult task of acquiring deeper futures on the final image [DOUGHERTY 2009].

Acoustic parameters

Material	Speed of sound, v (m s^{-1})	Acoustic impedance $Z = \rho c$ (10^6 kg m^{-2} s^{-1})	Attenuation coefficient at 1 MHz (dB cm^{-1})
Blood	1575 ± 11	1.62 ± 0.02	0.15 ± 0.04
Bone	3180–3500	4.8–7.8	14.2–25.2
Brain	1565 ± 10	1.54 ± 0.05	0.75 ± 0.17
Breast	1430–1570		0.3–0.6
Fat	1450	1.38	0.63
Peritoneal	1490		2.1
Subcutaneous	1478 ± 9		0.6
Heart	1571 ± 19	1.64	2.0 ± 0.4
Liver	1604 ± 14	1.63–1.75	1.2
Lung			40
Muscle	1581	1.70	0.96 ± 0.35
Soft tissue (mean)	1540	1.63	1
Air	331	0.0004	45
Castor oil	1500	1.4	0.95
PZT (lead zirconate titanate)	4000	30	
Water	1498	1.50	0.0022

Table 2– Acoustic properties of various materials (adapted from [DOUGHERTY 2009])

3.3 A-Mode image

A single transducer is used in this mode. The amplitude of the echoes received is displayed on the vertical axis, with the corresponding depth (dependent on the time of arrival of the echo) in the horizontal axis. The A-mode is useful in distance measurement (ranging), with applications in the detection of retinal detachment and the detection of the shift of the midline of the brain [RANGAYYAN 2005].

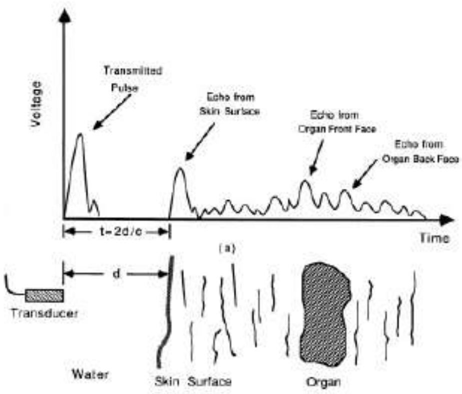

Figure 13–Schematic of A-mode imaging (adapted from DOUGHERTY, 2009])

3.4 M-mode image

This mode produces a display with time on the horizontal axis and echo depth on the vertical axis. The M-mode is useful in the study of movement or motion, with applications in cardiac valve motion analysis [RANGAYYAN 2005].

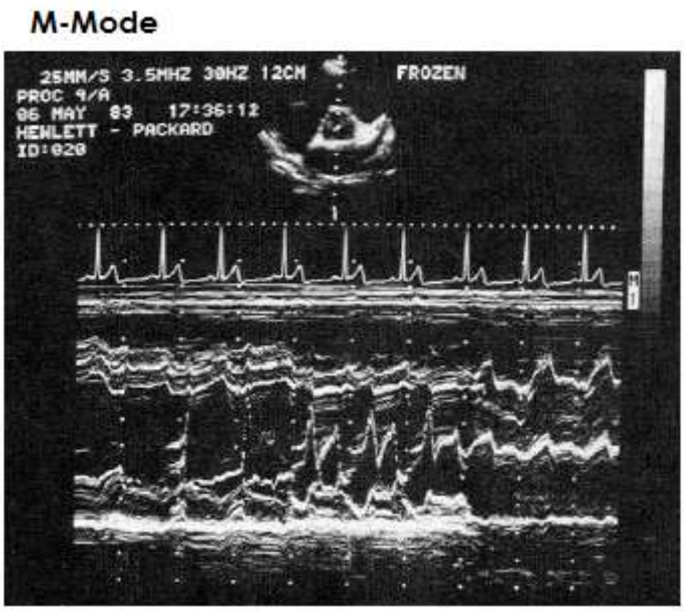

Figure 14– Example of M-Mode ultrasound imaging (adapted from PRINCE 2005])

3.5 B-mode image

This is the most typical image mode on ultrasound. It is used to produce a 2D tomographic projection of a medical image, through several sweeps. Each sweep is used to construct one unique vertical line in the final image, where the brightness of each pixel is given by the intensity if the echoes [DOUGHERTY 2009].

These multiple sweeps can be obtained mechanically, trough the rotation of the transducer or electronically, through the use of several piezoelectric elements instead of one. These elements are delayed from their neighbor, producing the direction of the image construction. After capturing all echoes in one direction, another direction is electronically defined, trough the introduction of these delays in the piezoelectric elements (figure 15) [DOUGHERTY 2009].

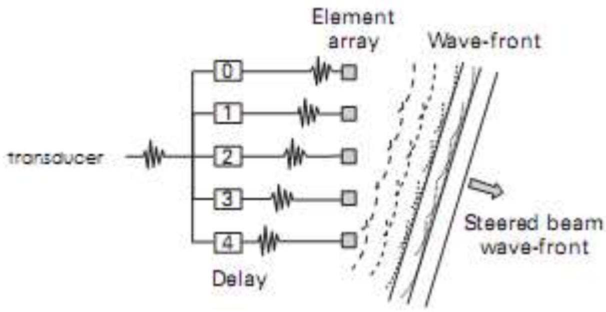

Figure 15– Schematic of B-mode imaging sweep (Adapted from DOUGHERTY, 2009])

3.6 Resume

In this chapter was reviewed the ultrasound system, explaining its basic principles, processes and imaging modalities.

The ultrasound imaging is based on high-frequency (1-10MHz) sound waves and their echoes to produce images that can demonstrate the organ movement in real time. Due to the sensitivity of the sound wave travelling through different organs, the output images have a high presence of speckle noise that prejudices the contrast of the images and makes their processing and observation difficult.

There are three common modes of this system, A, M and B- mode, which is one of the cheapest, armless and one of the most widely used image systems in the world. It is characterized by producing a 2D tomographic projection of a medical image, through several sweeps of sound waves.

Chapter IV – State of art on carotid image segmentation

Chapter IV –State of art on carotid image segmentation

4.1 Introduction

In the following chapter is presented the state of art on carotid image segmentation, describing several methods, and discussing the approaches given by different authors.

It will follow a time line, logic, beginning with the description of the oldest methods until it reaches the latest.

4.2 Edge tracking and gradient-based techniques

The first approach to perform carotid segmentation was based on edge-detection, aiming the IMT measurement. The observation of the ultrasound appearance of CCA drove this approach, assuming that CCA can be thought of as a dark region (lumen) surrounded by two double line patterns (carotid walls).

The distal wall IMT was measured by considering the intensity profile of a section of the image when moving from the centre of the vessel to the borders. This idea is illustrated in figure 16 where it begins by observing the original B-mode image in figure 16A. In figure16B the image shows a speckle removal, using filters based on local statistics. After that is visualized, in figure14C, the intensity profile related to the white dashed line shown in figure 16B. As we can see on this intensity profile, the adventitia layers and the lumen are clearly identifiable. The resulting of this intensity profile analyses is shown in figure14D, where it is visible the three interest points (AD_n, AD_F and L)on the original image [WILLIANS et al., 1992].

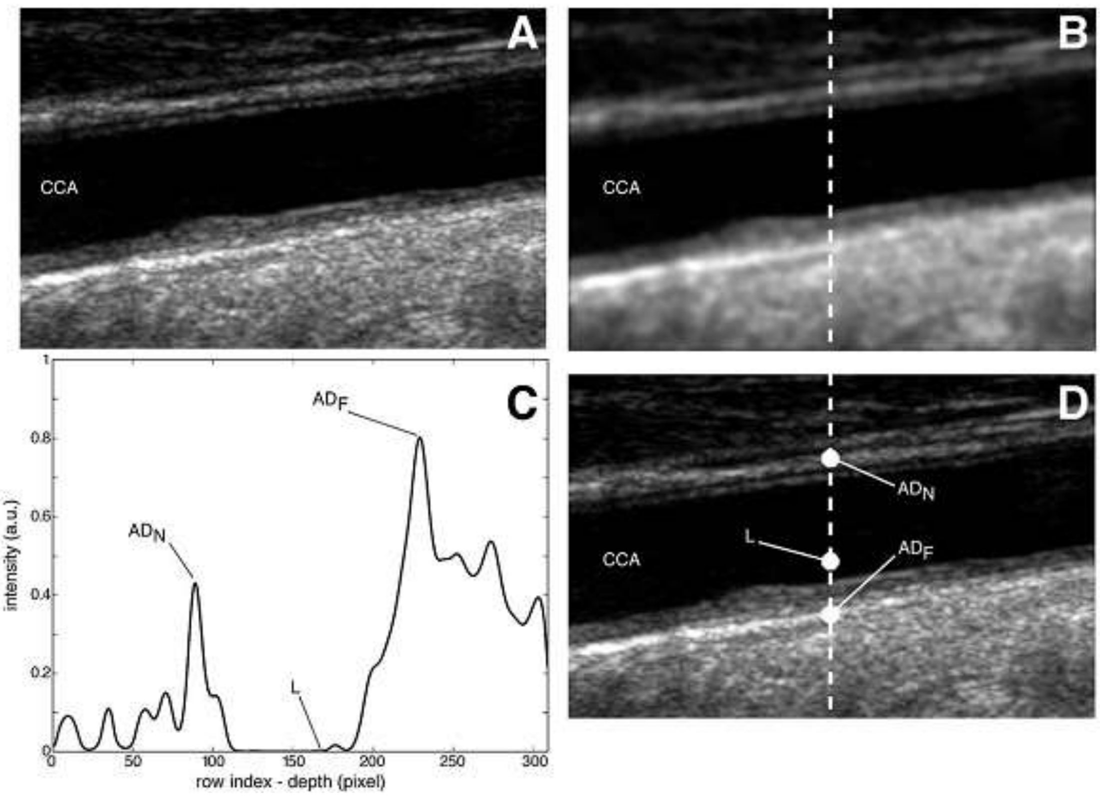

Figure 16– Edge-based detection method [MOLINARI et al., 2010]

The adventitia layer is usually very bright, being formed by dense and fibrous tissue. Therefore, it is relatively easy to find, on the intensity profile, the transitions between the lumen and the artery wall (LI) and then the transition between the media and the adventitia layer (MA). The distance between the two transition points constitutes the IMT estimate [TOUBOUL et al., 1992].

This was the structure used by Touboul et al. on the IMT measurement technique, applied in several multi-centric clinical and epidemiological studies.

In 2001, Liguoti et al. proposed a technique based on edge detection that used imaged gradients. The artery was considered horizontally placed in the B-mode image and for each column of the image they calculated the gradient of the intensity profile. It is assumed that all pixels of the lumen are black and the carotid wall layers are defined with gradient transitions, as we can see in the left panel of figure 17. The first set of transitions (20 to 40) corresponds to the near wall, the second (60 to 80) to the far wall. However, this ideal case does not correspond to the experimentally case, in which, the presence of noise, deforms the intensity profile, as we can see in the right panel of figure 17. For noise removal, the authors performed a statistical thresholding, before computing the image gradient. It was demonstrated that this approach had a negligible uncertainly of the IMT measurement (about 20μm), in clinical applications. Besides that, this technique lacks in full automation, once it is required to select the portion of the image that the approach will act, and it has bad results in identifying the carotid layers when the plaque has a smooth and regular surface [LIGUORI et al., 2001].

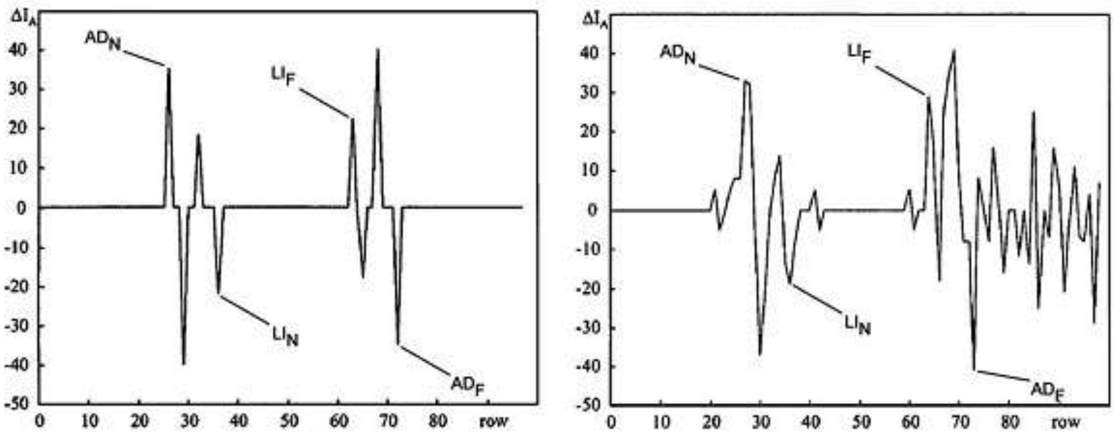

Figure 17– Carotid gradients **[MOLINARI et al., 2010]**

In 2005, Stein et al. proposed a gradient-based technique for measuring the IMT. This approach was not developed to perform a real carotid segmentation, but rather was a computer system to aid and improve the IMT estimation. By using an expert and one novice operator for performing several IMT measurements, with and without the aid of this system, it was clear that the computer-aided IMT measurements were faster, more reproducible, accurate and independent on the operator skill [STEIN et al., 2005].

Fatia, presented recently the most performing and innovative gradient-based approach. The major problem of the gradient-based methods is the high presence of noise in the image. In this study, the gradient performance was improved by the use of a first-order absolute moment edge detector (FOAM) and a pattern recognition approach. The FOAM operator was defined as:

$$e(x,y) = \frac{1}{A_{(-)}} \int_{(-)}\int \left|f(x,y) - f\left(x - \tau_x, y - \tau_y\right)\right| d\tau_x d\tau_y \qquad (4.1)$$

Where the original image f(x,y) is evaluated on a circular domain (-) of area $A_{(-)}$. This operator generically computes the mean dispersion of the values that the image assumes in that domain with the value that it assumes in the central point of the domain. After this step, the algorithm searches the maxima corresponding to the LI and MA transitions on the e(x,y) profile[FATIA et al., 2007].

This approach proved to have a very high performance on the IMT measurement, with a good robustness to noise, and was considered suited for clinical application. However, a few limitations were appointed, like the fact that the processing of curved vessels, or that does not appear as horizontal, may become difficult. It is not also a full automated process, once it is required that the user select a region of interest (ROI), that for sure, contains the carotid artery [FATIA et al., 2007].

4.3 Dynamic programming techniques

This type of technique was introduced in the early 1990s, in order to reduce the variability in ultrasound measurements.

In 1997, Wendelhag et al. introduced a dynamic programming procedure for automatic detection of echo interfaces, by using several features like echo intensity, intensity gradient and boundary continuity. These three features were combined in order to create a cost function. Each point of the image was associated with a specific cost, which correlated with the likelihood of that point being located at the echo interface [WENDELHAG et al., 1997].

Using a set of images, segmented manually by an expert, a ground truth was created to provide reference values. This reference was used on the training system that defined the weights of the cost function. The dynamic programming was then used to reduce the computational cost of the overall system, which was highly influenced by the number of points per image. The major advantage of this technique was full automation, since, the dynamic programming acts in every pixel of the image. However, the major limitation relies in the dependence on the ultrasound scanner and its settings, which demands a new training of the weighs, every time one of those two features changes [WENDELHAG et al., 1997].

In 2000, Liang et al. proposed a dynamic programming approach based on multi-scale analysis. This was basically an evolution of the previous approach. The dynamic system allowed that the localization of the position of the artery was performed by using estimation on a coarse scale and then refining the scale to estimate the precise position of the wall layers. This reduces the computational costs, as it used a coarse scale, and ensured the accurate performance, by changing to a fine scale where the wall location was estimated [LIANG et al., 2000].

4.4 Snakes-based segmentation

The snakes are deformable models that basically act like a set of vertices connected by line segments, which can evolve under the action of different forces.

Geometrically, a two-dimensional snake is a parametric contour represented by v(s)=[x(s), y(s)], where (x,y) refers to the special coordinates and s, represents the parametric domain. Therefore, the snake adapts itself by a dynamic process that minimizes a global energy function:

$$E_{snake}\,(v) = E_{int}\,(v) + ext(v) \qquad (4.2)$$

Where E_{int}(v) is the internal energy of the snake and E_{ext} (v) is an external driving energy. Usually the internal energy depends on some variables that are imposed to the snake and are defined as:

$$E_{int}(v) = \int_0^1 \{\alpha(s)|v'(s)|^2 + \beta(s)|v''(s)|^2 \qquad (4.3)$$

Where $\alpha(s)$ and $\beta(s)$ are the snake elasticity and rigidity coefficients, respectively. This energy provides control of the snake tendency to deform, so that it can be better suited to the need of each feature we want to segment.

On the other hand, $E_{ext}(v)$, typically depends on relevant features of the image (borders, lines, points, etc.). The snake points should evolve into the features of the image while remaining constrained by the internal forces. In the majority of algorithms, the external energy is modeled by using the local image gradients. This active contour reaches stability when Eq. (4.1) has his forces balanced. Therefore, snakes require a precise setup of their parameters in order to achieve that stability at the image relevant and desirable features.

However, some issues are considered, when developing a snake model:

- Need for optimization of the parameters;
- Dependence on the initialization of the snake points;
- Dependence on the number of points constituting the snake;
- Sensitivity to noise.

In 2002, Guitierrez et al. proposed an automated approach for carotid IMT and lumen diameter estimation, based on snakes and multi-resolution analysis. The active contour vertices could move being subjected to three different forces (internal, external and damping or viscous). The internal force was proportional to the contour curvature. The external force was the local magnitude of the image gradient. The damping force was proportional to the velocity of each contour vertex and in opposite direction. The use of the new parameter, the damping force, allowed this technique to smooth and stabilize the contour evolution. By using weighting factors, the authors were able to combine linearly these three forces and implement the approach. Although there is no information about the weights, optimization and the iteration conditions, the overall IMT measurement performance was relatively low and the contour validation was performed by comparison with human measurements [GUTIERREZ et al., 2002].

In 2002, Cheng et al. proposed a snake based technique for CCA segmentation, relying on the fact that traditional snakes could show poor segmentation performance in the region comprised between the intima and the adventitia layer, due to both being bright features. This erratic behavior can be shown in figure 18 [CHENG et al., 2002].

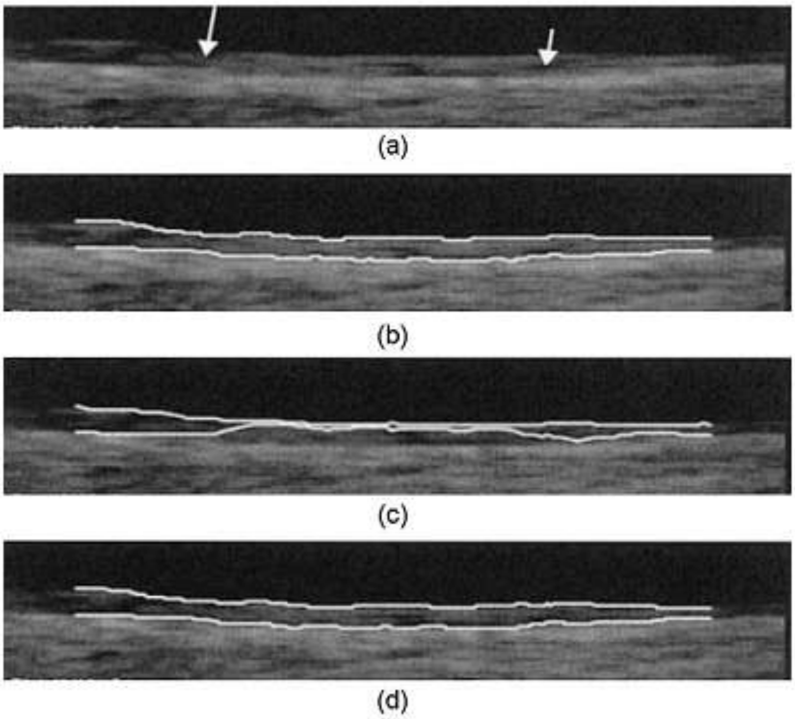

Figure 18– Erratic Snake behavior when segmenting LI and MA layers ([MOLINARI et al., 2010])

In figure 16(d) is visible the erratic behavior of the snake, when it is attracted by the noise super-imposed, and cannot segment correctly the target layers. To avoid this situation, the authors defined the external energy as:

$$E_{ext}(v) = -\int_{\Omega} g_0\,(|f_M * I| + D * I)ds = -\int_{\Omega} F(v)ds \qquad (4.4)$$

Where I is the original ultrasound image, f_M represents the Macleod operator, and $g_0$is the gravity constant (the symbol * denotes a bidimensional convolution). The matrix D is defined as:

$$D = A\begin{bmatrix} 0 & -1 & 0 \\ 0 & 0 & 0 \\ 0 & 1 & 0 \end{bmatrix} \quad (4.5)$$

where A is a positive weighting factor. As the central column of this matrix is a vertical gradient that has negative weigh upwards (-1) and a positive weight downwards (+1), it will be possible to prevent the possible trapping of the snake between the intima and adventitia layers, like is shown in figure 18(b), comparing with the ground-truth manual segmentation in figure 18(d)[CHENG et al., 2002].

This approach was then validated by comparison with human manual segmentations, by calculating the MSE of the distance between the computer-generated boundaries and the ground truth. This algorithm presents better performance than the previous; however, it still has a reasonable error, and also the issue of initialization was not addressed. Besides that the robustness to noise seemed adequate [CHENG et al., 2002].

In 2007, Loizou et al. overcome some snake limitations by realizing pre-processing standardization on the image, because most of the CCA segmentation techniques were lacking speckle noise reduction.

The authors begin by proposing preliminary image intensity normalization, followed by despeckeling. This normalization helped controlling the external energies on the layer boundary spots. Using a typical ultrasound image on 8 bit (256 levels of intensities), the approach re-scaled all the intensities, so that the median of the blood was between 0 and 5, while the median of the adventitia layer was between 180 and 190. The ideal snake parameters for this situation where$\alpha(s) = 0.6$,$\beta(s) = 0.4$ and $\gamma(s) = 2$ for the external force weighting. Despeckling helped to reduce the snake sensibility to the image noise, and allowed to improve the IMT measurement performance (validating with comparison to manual segmentation), comparing with the both previous methods. It was also presented an initialization technique that proved to be robust in presence of images with different noise level. However, a manual interaction was needed in order to seed points of the snake in the lumen [LOIZOU et al., 2007].

4.5 Local statistics and snakes

In 2007, Delsanto et al. proposed a combined approach of local statistics and snake-based segmentation, in order to obtain a completely automated segmentation algorithm [Delsanto et al., 2007].

The technique was divided into two distinct parts:

1) A module looking for the location of the carotid artery(local statistics);
2) A module looking for IMT measurement and segmentation (snakes).

To locate the CCA in the image, was proposed to cluster the image into a bidimensional histogram by computing the mean and standard deviation of the image pixels in a 10x10 neighborhood. This approach was based on the ideally homogeneous black lumen, which would be characterized by a very low mean and standard deviation. It is visible on figure 19 [Delsanto et al., 2007].

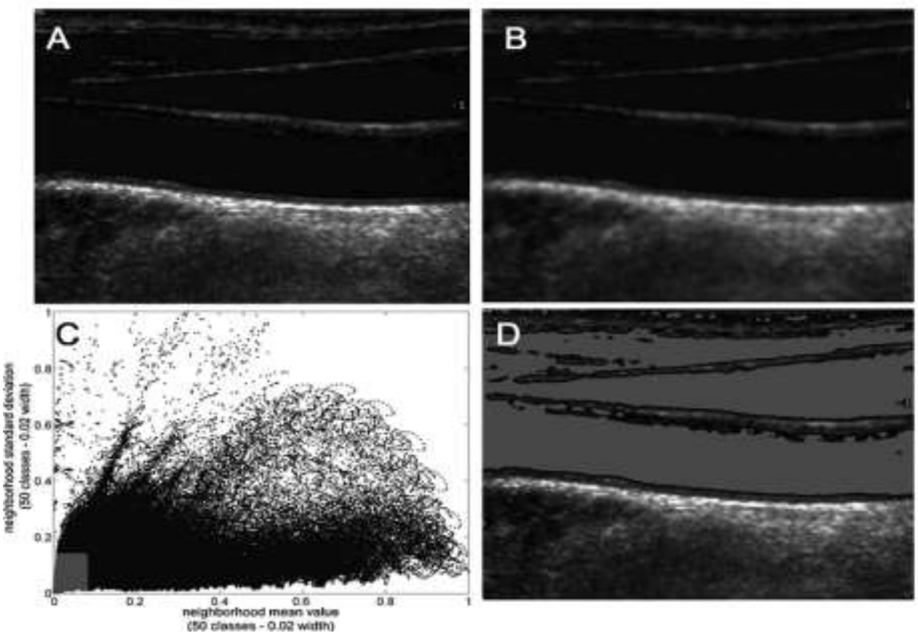

Figure 19–Delsanto lumen detection approach [MOLINARI et al., 2010]

In figure 19B it is visible the noise removal, comparing with the original image in figure19A. In figure19C is computed the bidimensional histogram between the mean and standard deviation of the predefined neighborhood of each pixel. The grey region corresponds to the region that was supposed to contain essentially lumen points. This result is also shown on figure 19D, where we can see the gray color defining the pixels previously detected [Delsanto et al., 2007].

Then the intensity profile of each column was analyzed in order to find the transitions corresponding to the near and far adventitia layers, which leaded to the tracing of these layers.

After the automated detection of the artery, the segmentation was based on an initial gradient-based contour, followed by a snake regularization and refinement of the LI and MA profiles. The snake formulation was defined as:

$$E_{int}\,(v) = \int_0^1 \frac{1}{2}\alpha(s)|v^{'}(s)|^2 + \gamma(s)E_{ext}\left(c(s)\right)ds \qquad (4.6)$$

where $\alpha(s) = 0.1$and$\gamma(s) = 0.01$.

This approach was also validated using comparison to the human manually segmented image, and besides it produces similar results to the previous method, it has the advantages of being a full automated approach, and having the ability to adapt to any kind of CCA projection despite their curvatures [Delsanto et al., 2007].

In 2008, the same group of authors proposed an improvement of the technique that could also segment the near wall as well as diseased vessels. The location of the artery was identical to the previous approach, and once it was detected, a ROI was defined, through the use of the near and far adventitia profiles. A fuzzy k- means classifier was inserted in the segmentation module in order to cluster the ROI pixels. There were considered three different cluster for lumen, intima and media layers. Then, snakes were used to refine the LI and MA boundaries. Using also the MSE to evaluate the performance, the authors obtained reasonable results. Relating to the new feature improvements, it was shown that it is a robust algorithm in segmenting plaques (stable and unstable) [Delsanto et al., 2008].

This approach was further developed by Molinari et al. being the last results shown in figure 20.

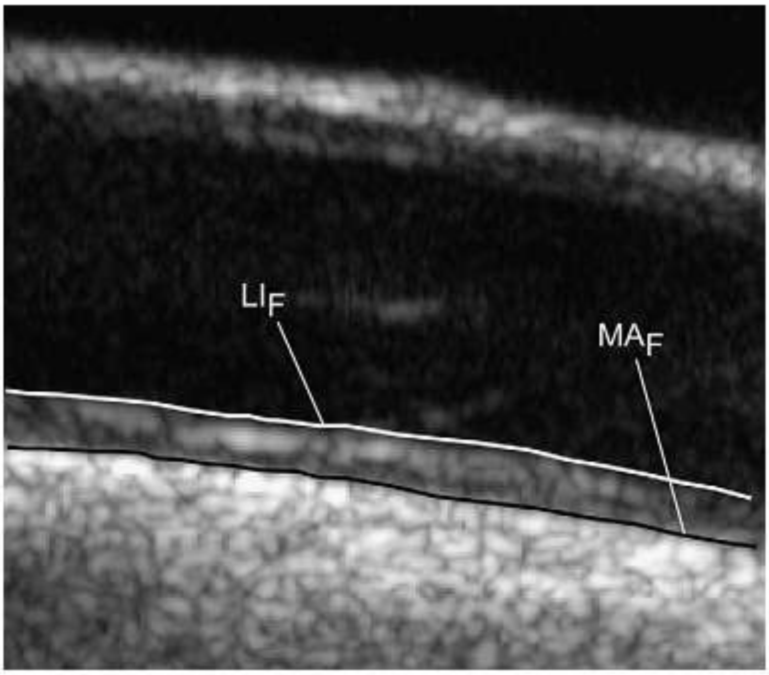

Figure 20–Molinaryapproach [MOLINARI et al., 2010].

4.6Nakagami modeling

This approach used the modeling of the intensity of a small ROI image to perform the segmentation. It was assumed that if a ROI window contained the carotid wall, then the intensity was characterized by a specific pattern and the presence of speckle noise [DESTREMPES et al., 2009].

Destrempes et al. proposed a segmentation approach based on the Nakagami mixture modeling and stochastic optimization. They considered small vertical ROI (Stripes), contained the IMT complex and analyzed the radiofrequency signal. The upper panel of figure 21 shows one sample from this method [DESTREMPES et al., 2009].

The vertical RF signals were analyzed considering three assumptions:

1) The lumen corresponded locally to the distribution with lower mean;
2) The IMT corresponded locally to the mixture;

3) The adventitia corresponded locally to the distribution with higher mean

The lower panel of figure 21 shows the assignment of the four profiles to the lumen, intima-media, and adventitia boundaries. Firstly, they computed the maximum a posterior estimator of the proposed model, using the expectation maximization algorithm. The optimal segmentation was achieved using a variant of the exploration/selection algorithm, and the convergence was assured asymptotically and independent from the initial solution. This technique proved to have very high performance rates in CCA segmentation and the mean absolute distance metric was used to obtain the LI and MA segmentation errors [DESTREMPES et al., 2009].

The assumption 3) makes this technique little applicable in processing a generic pathology image. In a presence of calcified plaque, the adventitia might not represent the local distribution with higher mean value, also the authors admitted that theirs method was well suited to a semi-automatic context that required minimal manual initialization [DESTREMPES et al., 2009].

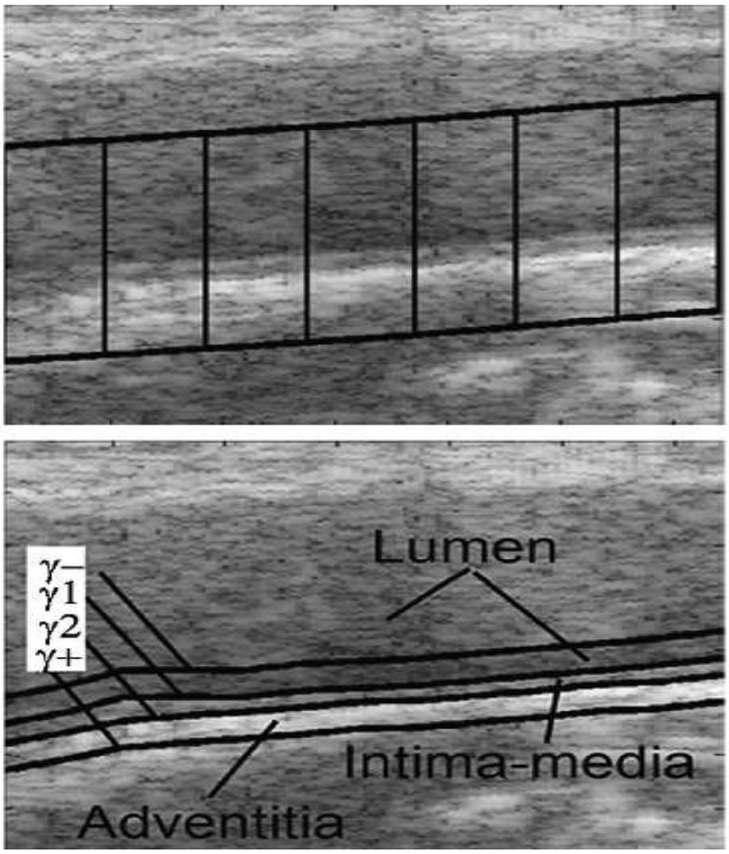

Figure 21–Nakagami-based approach [MOLINARI et al., 2010]

4.7 Hough transform (HT)

Between 2004 and 2009, Golemati et al. developed a segmentation algorithm based on the Hough transform. This transform is normally used to detect lines and circles, and the authors exploited his properties in order to develop a technique that can both segment longitudinal and transverse B-mode carotid images, assuming that the CCA layers are straight in longitudinal projections and circular in transverse projections. The dominant lines in longitudinal images, belongs to the LI and MA boundaries and the distance between them was taken as the IMT measurement. The same approach was used on the transversal images, but using circles instead of lines, resulting in the extraction of the LI and Ma layers. This technique is shown in figure 22 [GOLEMATI et al., 2007].

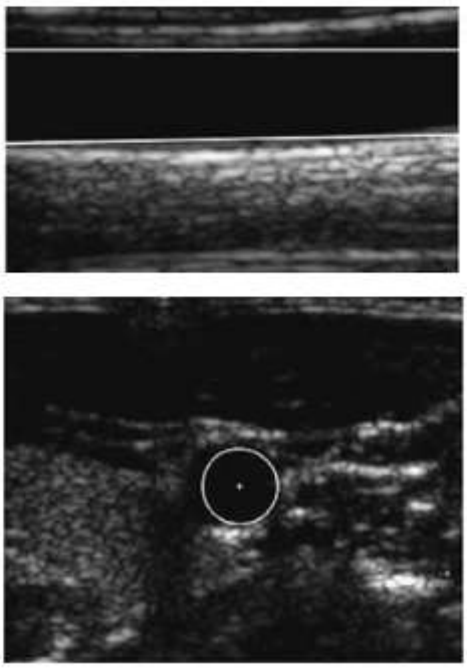

Figure 22–Hough transform approach applied to the CCA segmentation [MOLINARI et al., 2010].

This technique was also shown to be helpful in images with small wall plaques; however, they have a clear limitation related to the shape of the artery. The horizontal disposition and the straight form must be present for a successful segmentation. The validation of this technique was realized using cross-reference from human tracings, and producing good results in the sensitivity and specificity features [GOLEMATI et al., 2007].

4.8 Integrated approach

Molinari et al. developed a generalized architecture for vessel wall segmentation in 2009, consisting into two parts:

1) A module for the automatic location of the CCA in the image
2) A segmentation procedure that automatically traces the LI and the MA contours of the far wall once CCA was localized.

In step one, the local intensity maxima of each column are processed by a linear discriminator to detect which were located on the CCA wall. These detected points are used now as seed points for the present methodology, as shown in figure 23B. By linking them, line segments are now formed, followed by an intelligent procedure that removes short or false line segments and joins close and aligned segments, avoiding the over segmentation of the carotid wall. The result of this procedure is shown in figures 23C and 23D, it is visible the result after the joining of the segments detected. Once the CCA is detected, the algorithm will scan the intensity profile for each column of the image, being classified by the use of a fuzzy k-means classifier. The classifier is initialized by the intensity values and has only 3 clusters (lumen, intima and media layers, and adventitia layer). The points between the transitions of these clusters are taken as the LI and MA boundaries [MOLINARI et al., 2009].

This is a fully automated technique, which the integrated morphological procedures allow very good results in CCA segmentation, achieving a 95% success rate in the cases (validated by human tracing comparison). The performance metric was defined by the mean absolute distance, which led to a high error for the LI and a low error for MA boundaries. This result with the LI, make the error of the overall IMT measurement high then the previous techniques [MOLINARI et al., 2009].

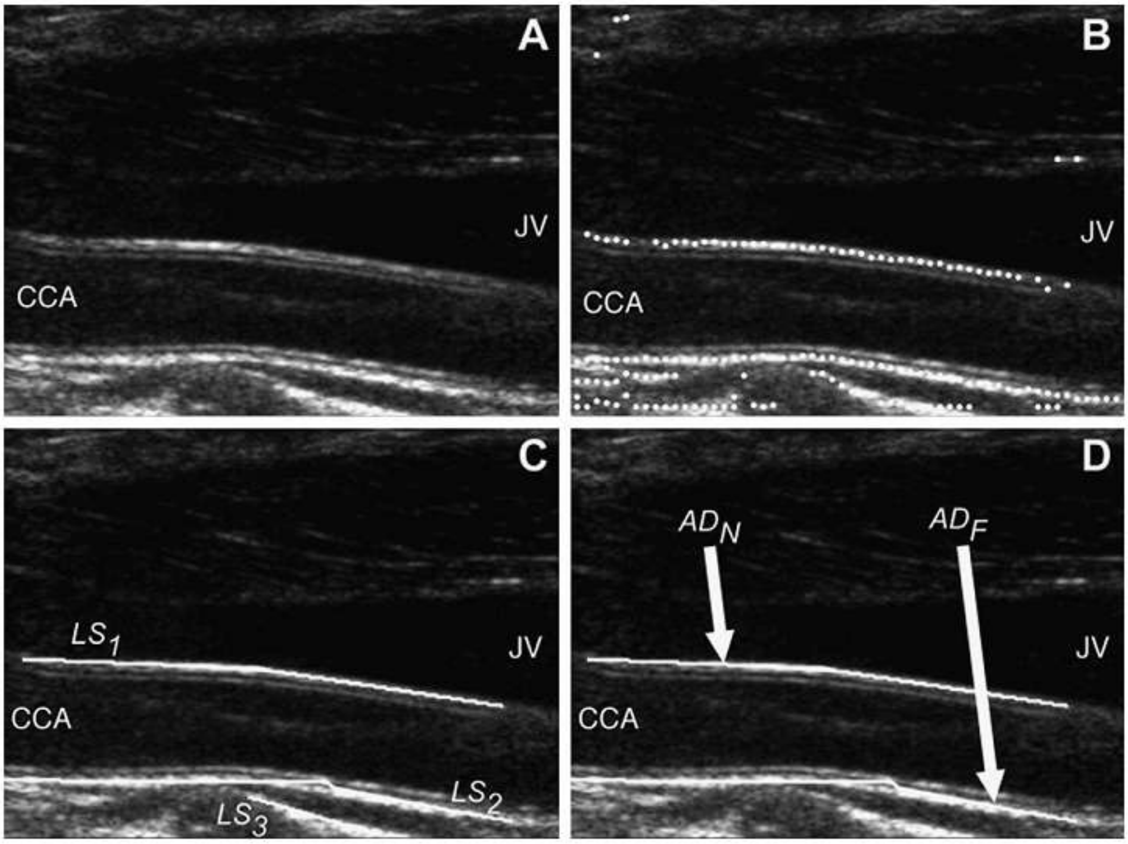

Figure 23– Molinari integrated approach [MOLINARI et al., 2010].

4.9 Resume

This chapter reviewed the state of art on carotid image segmentation, describing several methods, and discussing the approaches given by different authors.

The edge and gradient based method is computed, assuming that CCA can be thought of as a dark region (lumen) surrounded by two double line patterns (carotid walls), creating a huge gradient in these areas.

The Dynamic programming technique is based on an automatic detection of echo interfaces, by using several features like echo intensity, intensity gradient and boundary continuity.

The snakes based- segmentation uses deformable models that basically act like a set of vertices connected by line segments, which can evolve under the action of different forces.

The local statistics and snakes based approaches combine the two techniques in order to achieve a completely full automated detection.

The Nakagami modeling is based on the modulation of the intensity of a small ROI image to perform the segmentation.

And finally, the integrated approach developed by Molinari is based on a module that automatically detects the location of the CCA in the image and then performs a segmentation of the wall of the CCA contours.

Chapter V – Methodology

Chapter V – Methodology

5.1 Introduction

In this chapter is presented all the steps of the implemented method to segment the lumen boundaries and its 3D representation. Each step is detailed with schemes and images illustrated their actions and main issues. As it is a novel method, some of the images used are provided by the method itself.

5.2 Pre-Processing

Due to high present of ultrasonic speckle noise in the images, it is essential that some denoising process is applied on them. The anisotropic diffusion operates as a local coordinative transformation using first and second order normal derivatives of the image. This anisotropic diffusion acts on the domains of edges and local details, diffusing along the tangent direction of edges.

P. Perona and J. Malik give us the equation to smooth a noisy image:

$$\frac{\partial u(x,y,t)}{\partial t} = div(g(|\nabla u(x,y,t)|)\nabla u(x,y,t),$$

where u(x,t,y):Ωx[0,+∞)→ R is a scale image, g(| ∇u |) is a decreasing function of the gradient [SHUJUN 2006].

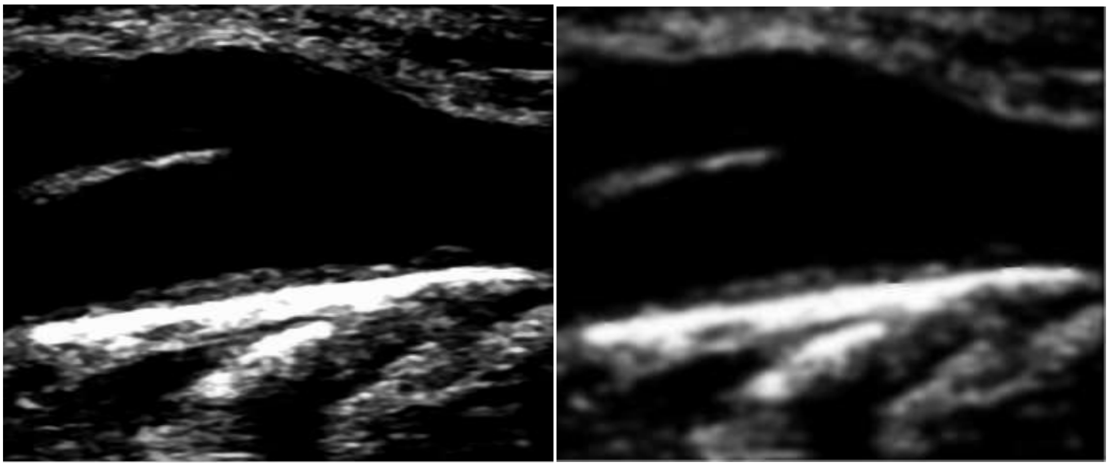

Figure 24–On left image is the result of the anisotropic diffusion filter applied to the right image

5.3 Inner Lumen Points

The first step into the lumen boundaries segmentation is necessarily the detection of inner lumen points, which in practice will work as seed points. This method is based on the habitual hypoechogenic feature (dark region) of the lumen section [ROCHA 2010]. Also, this procedure is fully automated, and it detects lumen points despite the object orientation.

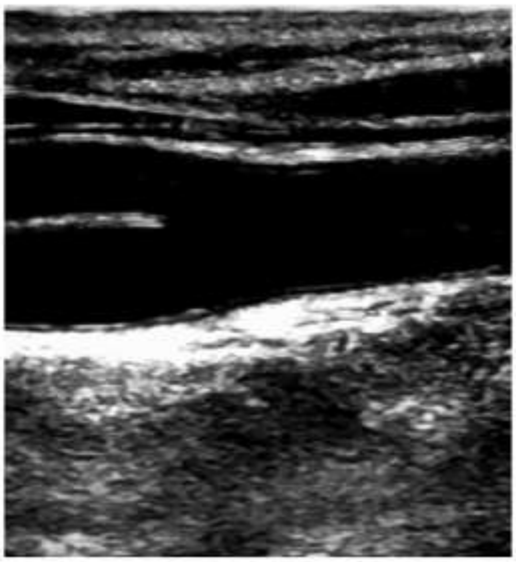

Figure 25 – Carotid ultrasound visualization

As we know the lumen is one of the biggest structures of this type of images type, so in order to search representative pixels of hypoechogenic regions a closing morphological operation is performed (disk with size=20), so only the stronger and biggest target regions remain fully distinguished, as we can see in figure 26.

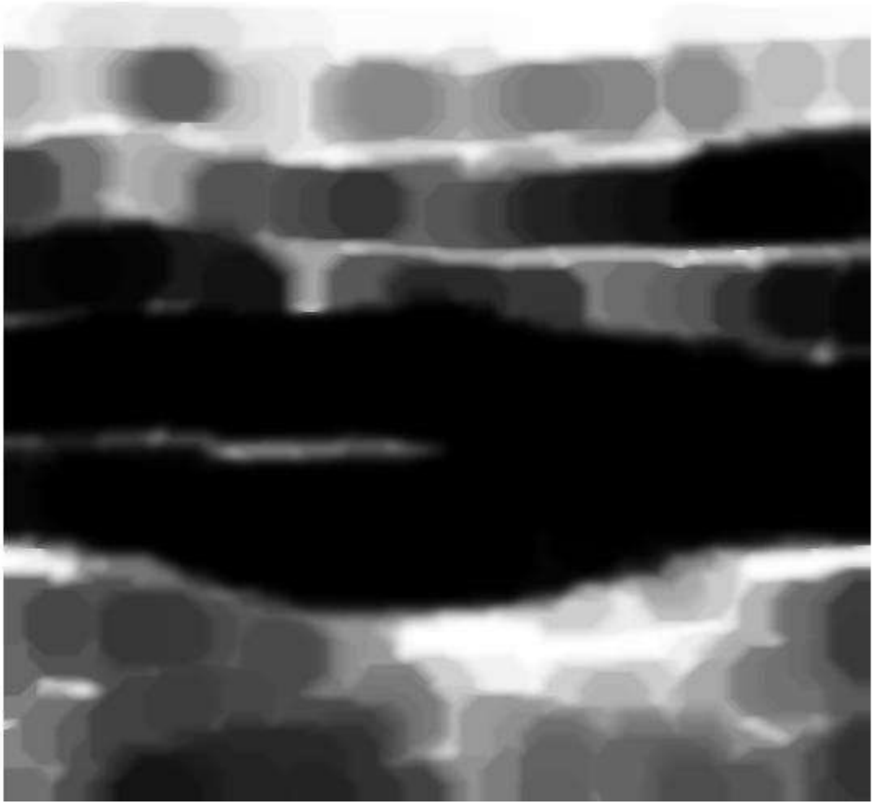

Figure 26– Closing morphological operation results (disk with size=20)

With these results, the next step is simply look for the significant pixels that meet the criteria. To accept a certain pixel as a lumen point candidate, it is required that in a row by row search for a relevant sequence (higher than N) of pixels with intensity bellow ξ ($p(n,m)<\xi$), where n= row and m=line) is detected.

On the presence of a positive detection, we assume that the middle pixel point of that sequence is a suitable lumen inner point candidate.

For example, if in row n a sequence of k points, where k>N and p(n,m)<ξ, is detected with a start point in line mi, the lumen inner point candidate in that sequence is the pixel p(n,mi+(k/2)), located in row n and line (mi+(k/2)).

As we can see in figure 27, the red points illustrate the inner lumen point candidates and they are a match with the visual black region centers, in a row by row view. This approach allows the method to be sensible and accurate to the lumen orientation variation.

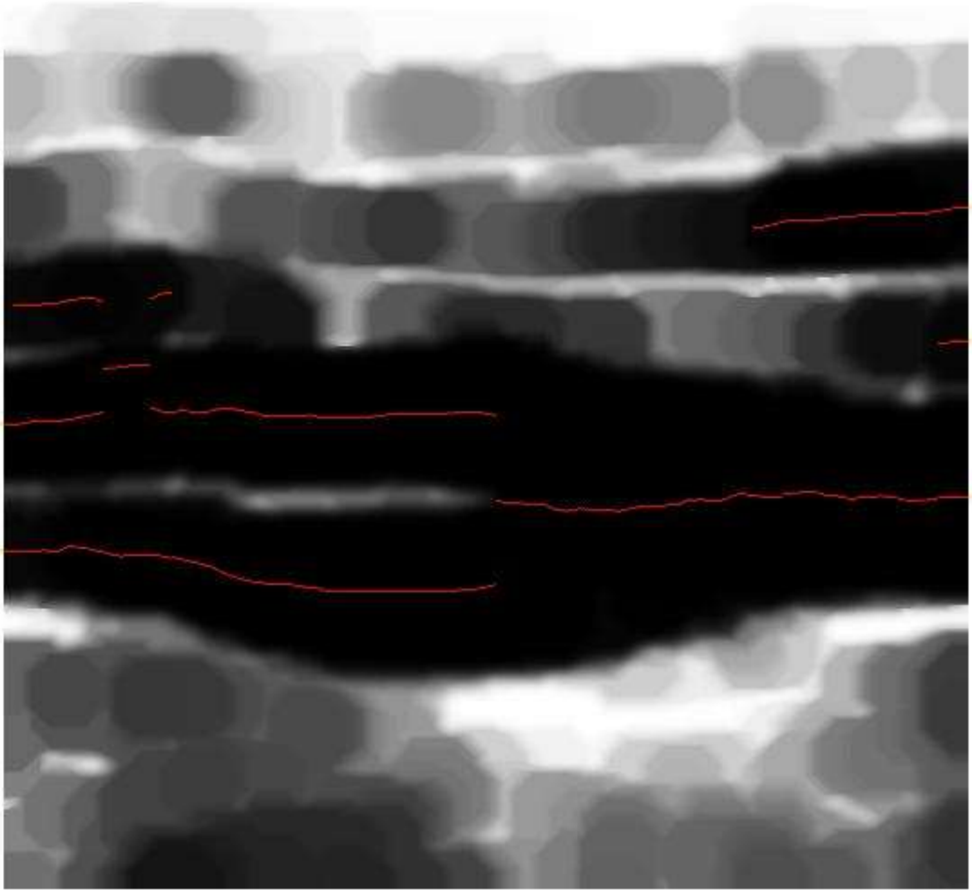

Figure 27–Inner lumen points candidates (red points)

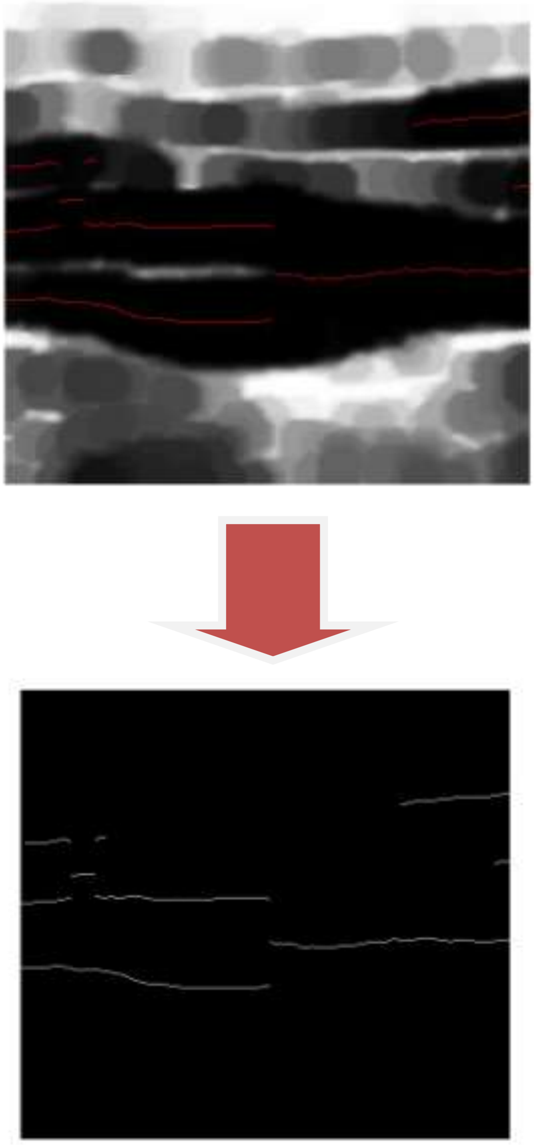

Figure 28 – Candidate points separation

With all the detected points extracted (figure 28) they will form groups of segments, but it may be possible that not every one of them actually belongs to the lumen, so in order to bypass this situation a final selection, of inner lumen points, must be performed.

Firstly, the points previously detected are divided into several groups or brunches. Each group is going to be a segment, whose points are connected sequentially by an 8x8 neighborhood; however, there are some segments that in practice are separated by small gaps, and it may induce errors. For example, on figure 29(a), there is a situation where two segments, which are supposed to be just one, are separated by this kind of gap. To solve this problem, another closing operation is implemented so these little gaps that may exist get closed, and the smaller significant segments saved (figure 29(b)). It is important that the structuring element of this morphological operation is just as small as it is required so it does not merge undesired segments.

(a)

(b)

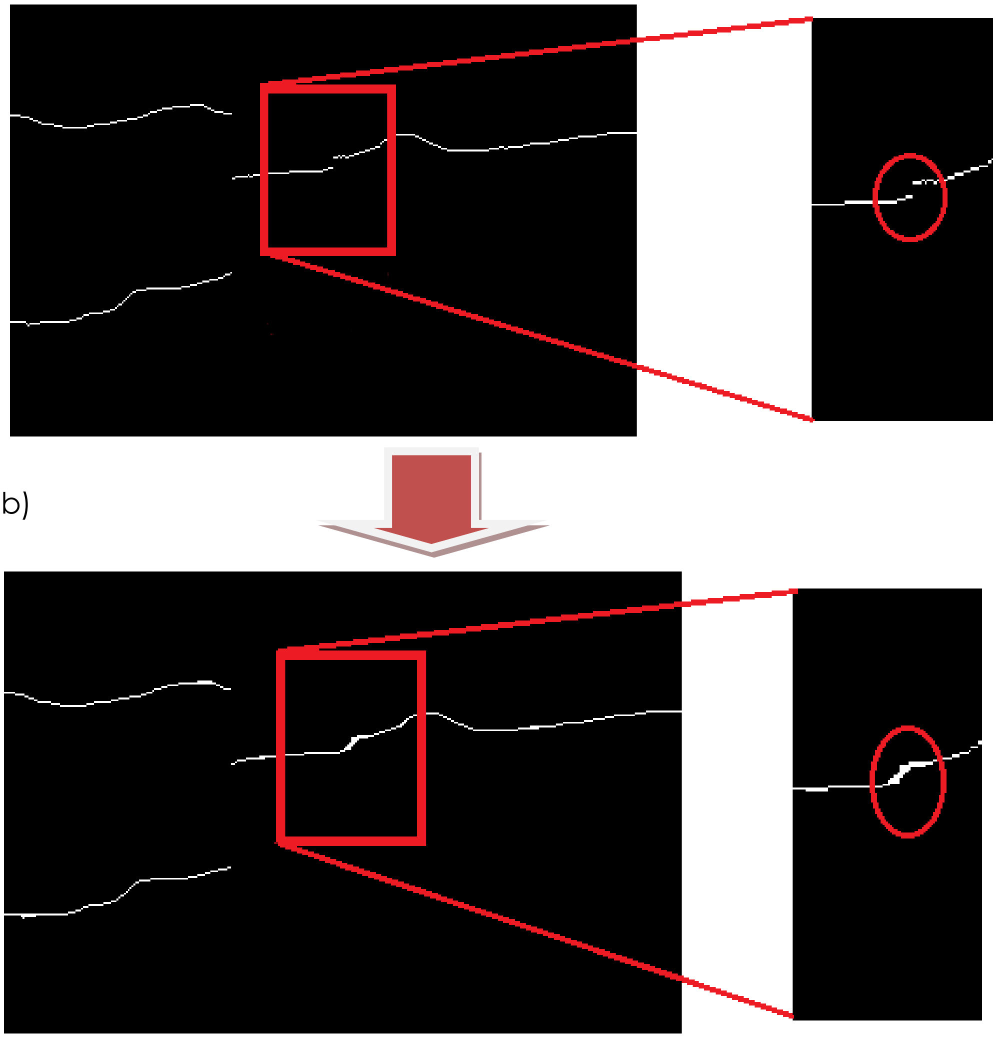

Figure 29–Small gaps correction example: (a) Target gap identification, (b) Gap correction

Another step to dismiss false lumen points is building a ROI centered on the lumen region. This will lead that the farthest segments from the lumen region get ignored, and the algorithm focus remains only on significant areas. The main problem with the ROI is that first, we need to knowledge where is located the lumen region. In order to achieve this, we will use the CCA brunch, which is assumed to be the strongest one and located on the right side of the image (figure 30).

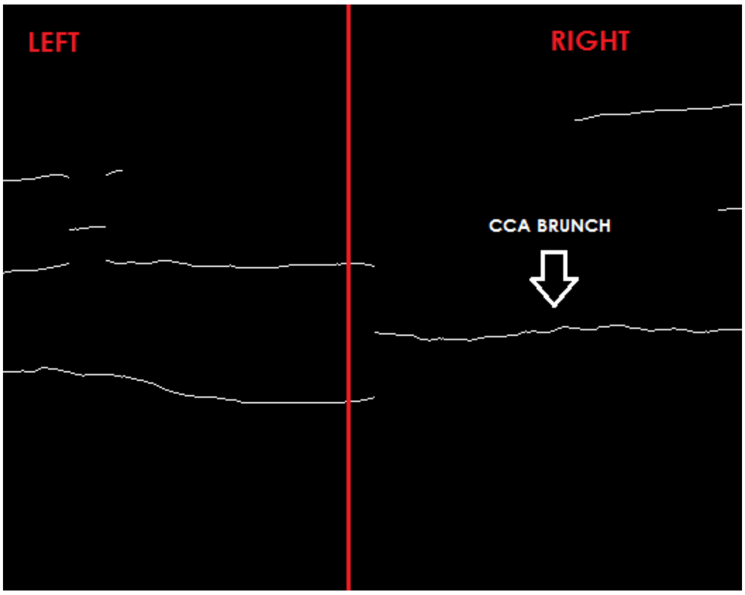

Figure 30– Full image division exemplification and CCA segment identification

In practice, this method searches on the right side of the image the strongest and biggest segment detected, removing all the others (figure 31). This search location works as an individual image, and the only thing that matter is to find the location of the segment that best represents CCA inner lumen points, so the information removed in this step does not influence the data of the full size image.

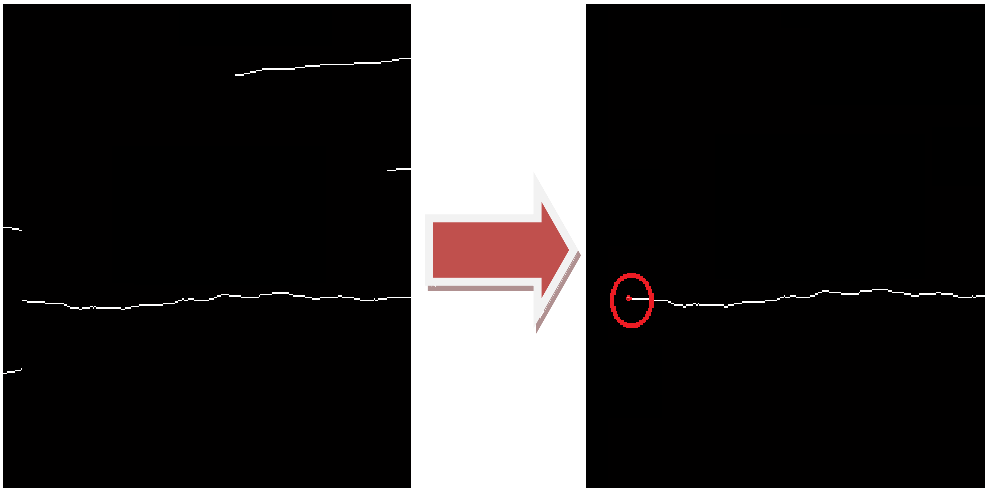

Figure 31– Detection of CCA segment location and ROI central range point(the red circle and the red dot indicates its location)

When the target segment is found, the ROI criteria are built based on the position of the nearest point (pixel a) of that segment to the rest of the image (left side). From this position only the pixels, between a certain horizontal (lines) distance, are considered (figure 32). This feature is important due to the variable carotid orientation. Not every lumen is disposed straight on the horizontal axis, as some of them may have curves or have an ascending or descending development. Theoretically, the closest points to each other have a smaller deviation than the farthest ones. This is why the nearest point to the left side of the image is used to build the ROI image, as it has the theoretically small deviation.

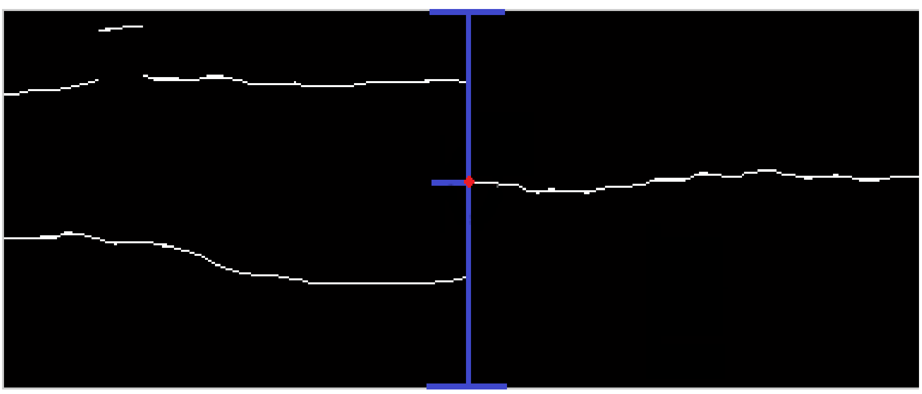

Figure 32 – Scheme of ROI definition (the red colored point is the nearest point of the CCA segment to the left side of image and the blue colored lines, defines the ROI extension)

Normally, the false lumen points are located on the smaller segments, as shown in figure 33(a), due to a better definition of the hypoechogenic features on the lumen region. These segments can be easily identified by simple pixel quantification. The segments composed by a number of pixels smaller than a certain size β, are removed from the image, as shown in figure 33(b).

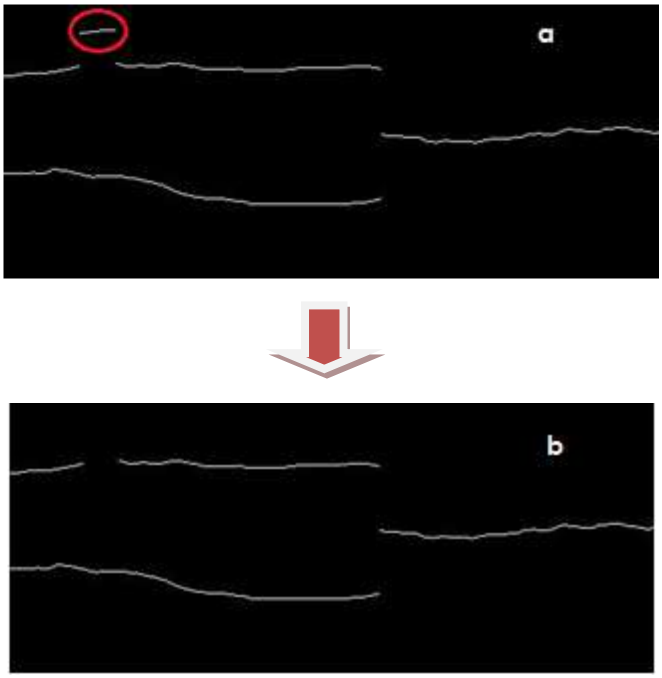

Figure 33– False Lumen inner segment detection and removal

At this stage, we have only segments that belong to the lumen; however, some of them may have gaps, which are bigger than the previously closed. This happens due to the present of false segments that induces errors and also to the fact that the first gap correction is only directed to small gaps, in order to avoid that those false segments merge with the real ones. Remaining only real segments, a higher closing criterion may be implemented. The structural element used in this closing operation is based on lines with several orientations, so it can fulfill the gaps of every segment no matter what spatial disposal they have. In figure 34 it is visible the result of the closing operation applied to the image on figure 33.

Figure 34– Result of Gap fulfill of the image in figure 30

Due to the morphological operation, a thickening process occurs on the segments. As there is only needed one point by row, for each segment to define it, the other points in that row and for that segment are going to be deleted. To implement this operation firstly we need to know if we are in a presence of a bifurcation area or on a single vessel area. This is achieved by quantifying the number of segments, so if it has more than one it means that we are in a presence of the first area, otherwise it means we are in presence of a straight lumen area.

In the case of a single vessel area, a single run is performed and the undesired points removed. That run is basically a search row by row for the first pixel that belongs to the segment. That pixel is saved, and all the others behind it deleted. In the presence of bifurcation, other precautions must be taken. Two different runs are implemented in this case. The first is exactly equal to the single vessel run as it takes the upper points on the image it will cover the CCA segment and the external segment (figure 35); however, the run for the internal segment is performed on a backward direction, starting in the end of the image and coming up until it reaches the targeted point (figure 35). This run is applied only until the row of pixel a, because it is known that this specific row corresponds to the beginning of CCA segment and the end of the internal and external segments.

The final result of this method applied to the image is shown on figure 37.

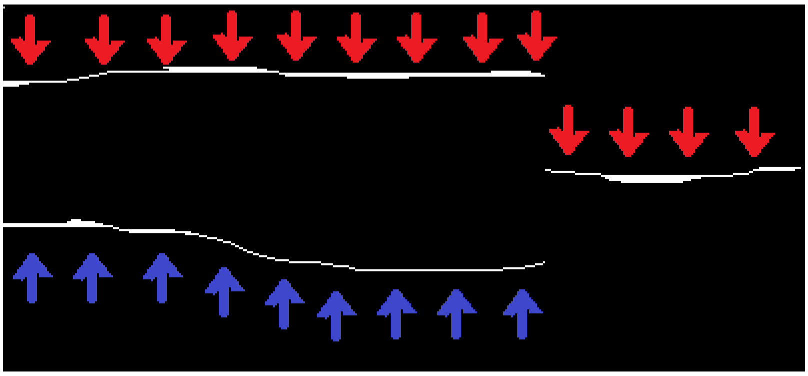

Figure 35– Red colored arrows belong to the first run and the blues ones to the second run

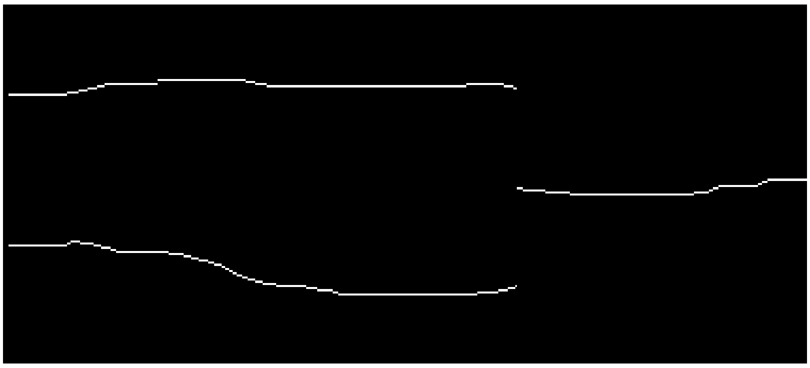

Figure 36– Final result of lumen points detection

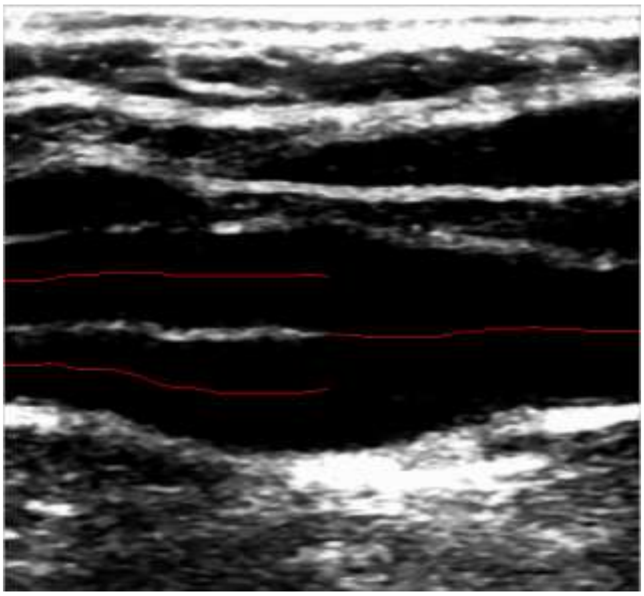

Figure 37– Visualization of the detected lumen inner points

5.3. Multi-Scale Lumen Boundaries Segmentation

The ultrasound imaging of the carotid artery may incise only on the CCA, or it can incise also on the bifurcation of the CCA, a sensitive point of this artery. The first case there are only two portions of the lumen to detect, the upper one and the lower one, while on the second case, somewhere in the image, a central portion appears, as it divides the external and internal arteries (bifurcation), like shown in figure 38. In the last case, besides the upper and lower portion, there is also a necessity to detect the central portion of the lumen walls.

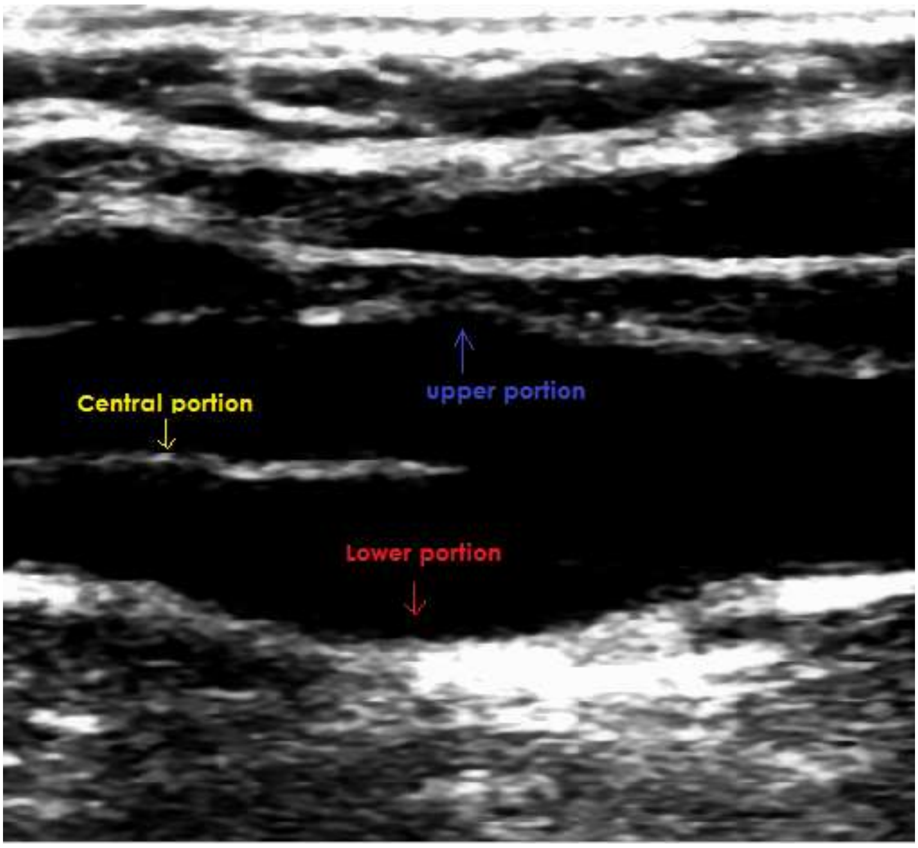

Figure 38– Lumen walls

It is known that the intima layer has a much higher intensity than the lumen area, so it is expected to find, in those transition locations, a presence of a strong magnitude gradient. Based on this, and using the lumen inner points as seed point, several row by row runs are going to be performed in order to find those strong gradient points. For each seed point, it is expected to find two associated points, one superior to that point and the other inferior, which are a match to the nearest lumen walls. The differences between the runs of the two types of image can be found on figures 39 and 40.

This approach is based on a median filter (with different sigma) applied to the image, followed by a gradient calculation, performed with a sobel operator. Normally, the different walls of the lumen, in a single ultrasound image, show that the lower portion has a better contrast and definition than the upper one (figure 41). It is a fact that the speckle noise induces more errors on the upper portion than in the lower. Based on that, it is clear that the results of the same filtering rate have a higher deformation on the first portion than on the second, leading the lower one to lose some significant data that may induce errors on the segmentation (figure 41). This supports the multi scale approach used in this method, which the main goal is to maximize the relation between the noise and significant data removal.

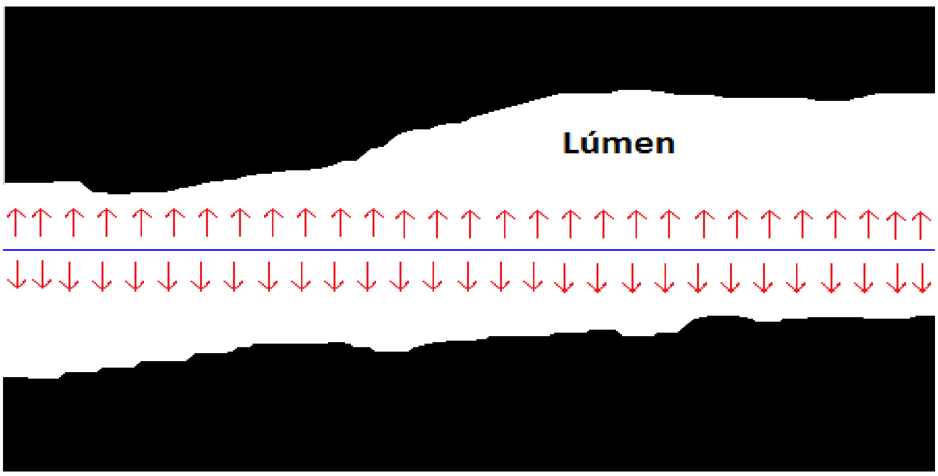

Figure 39– Scheme of the lumens walls search on the CCA

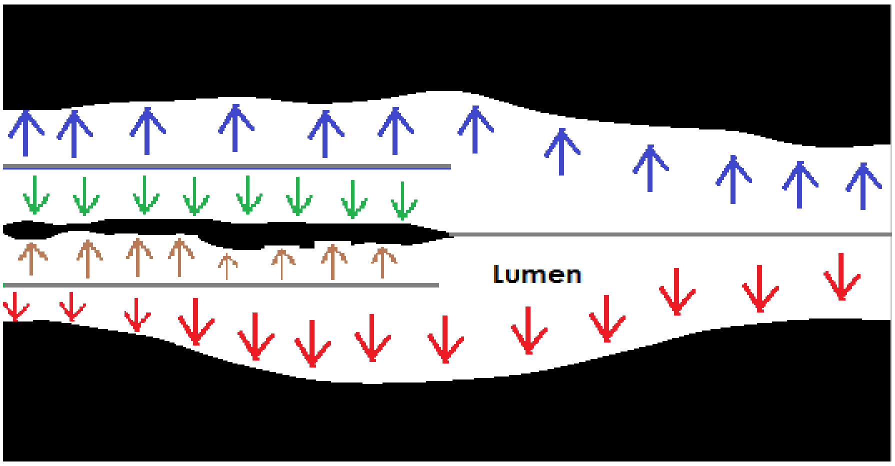

Figure 40– Scheme of the lumen walls search on the bifurcation area

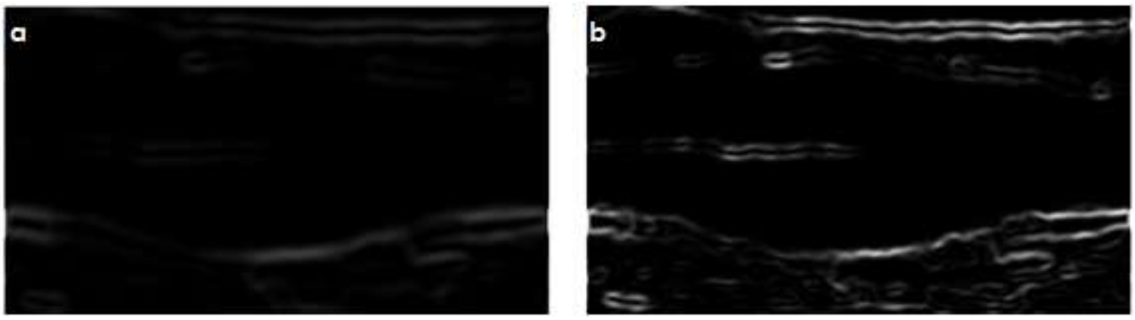

Figure 41– Images with different sigma applied on the median filtering, offers different results;(a) has a higher sigma, thus the lower part shows a smother lower portion with less noise interference than in (b); however, the upper part in (a) is highly erased. A single sigma is not fit to take the best of each portion as the lower portion has better results in (a) and the upper in (b).

In practice a higher sigma, on the median filtering process, is applied to the lower portion (figure 41(a)), as it can handle higher deformations, while keeping the major significant data information and a smaller sigma is applied to the upper portion (figure 41(b)). In this case, there is a lower noise removal, but the most important data is actually saved. Note that in case of a bifurcation, the central portion, although it has a good contrast and low noise rate, due to the presence in the middle of a huge hypoechogenic area (lumen), it has also a little number of pixels defining it, so this portion will also need an even smaller sigma so the error is minimized. And that has some logic, because as said before it also has less noise interference.

In order to retain only the strongest gradient points, only those who have a higher value than δ are kept. The importance of this operation is shown on figure 42.

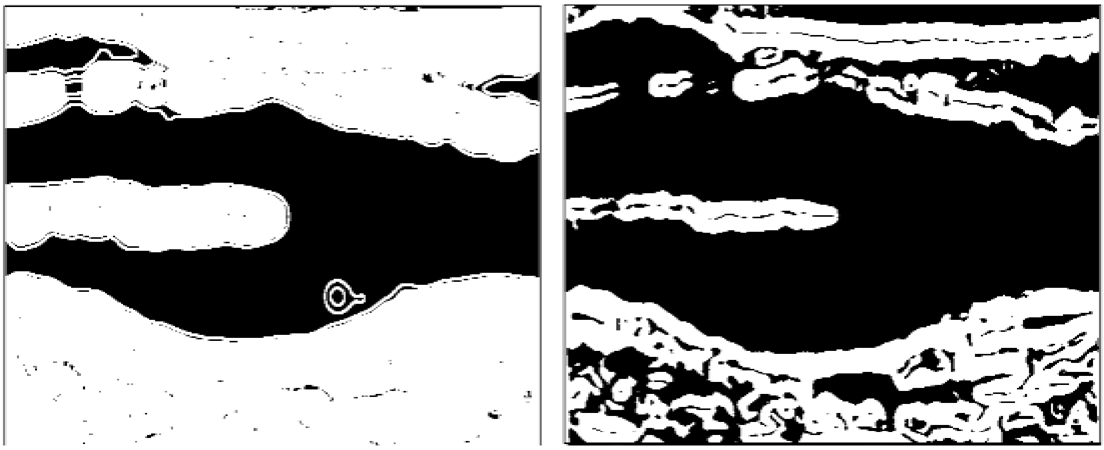

Figure 42–The first image shows the binary result of the sobel operation and the second image shows the binary result of the first image thresholding

Now the runs specified in figure 39 and 40, are applied on the data of the previous threshold results. As each portion has a different run, the final result is a combination of all of them into the original image, like shown in figure 43.

In figure 43 it is also visible that some segmentation errors may be found in the results, especially on the upper portion, like gaps between segments or false lumen walls detected. On the lumen inner points detection the errors were solved by using morphological operators and removing small segments; however, in this case, a different approach is used. As the major part of the lumen walls is defined, it is applied a median filter to the segmented combined results (figure 44) and then only the stronger point in that row and for that portion is kept. This selection is performed by a peak search on the intensity profile of that specific run. For example, on figure 45, the algorithm is performing a run on the upper portion, and the orange line represents the target row and its length. On the right, it is possible to see its intensity profile, with the red cross signalizing the higher pixel in that run. That pixel is going to be the chosen one to define the lumen upper portion boundary in that row. In figure 46, it is visible the final result of this operation.

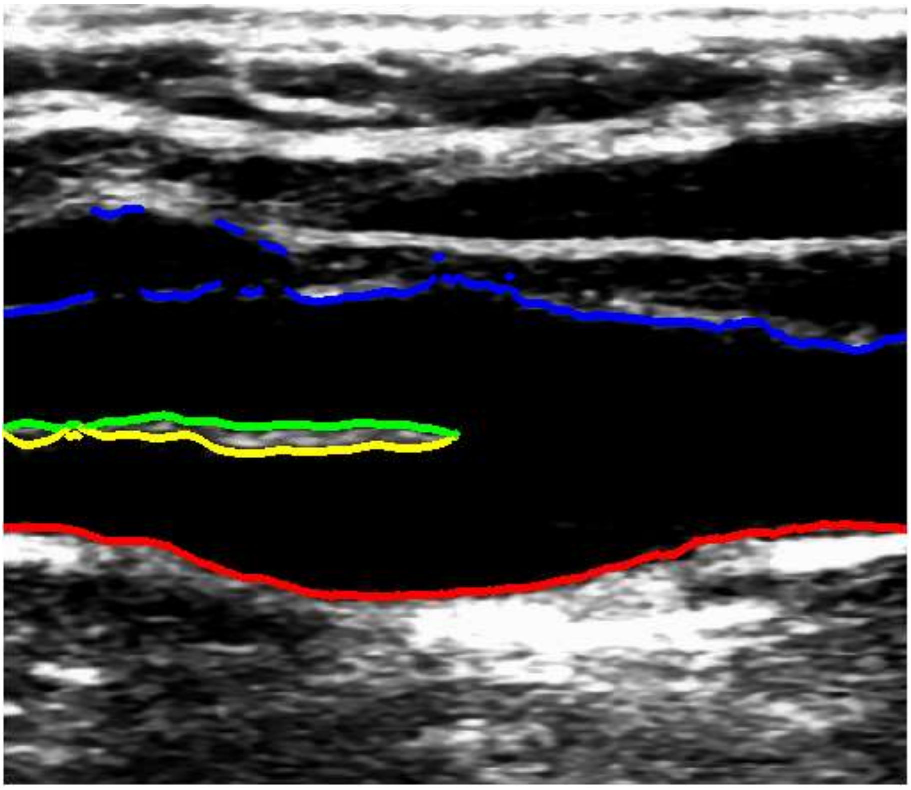

Figure 43– Combination of the results for each portion

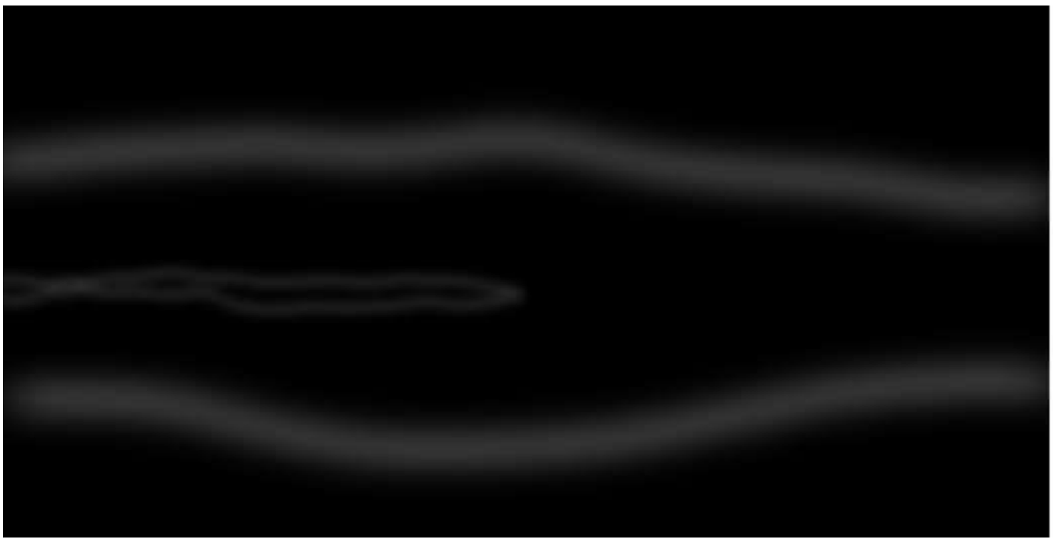

Figure 44–Smoothed lumen limits.

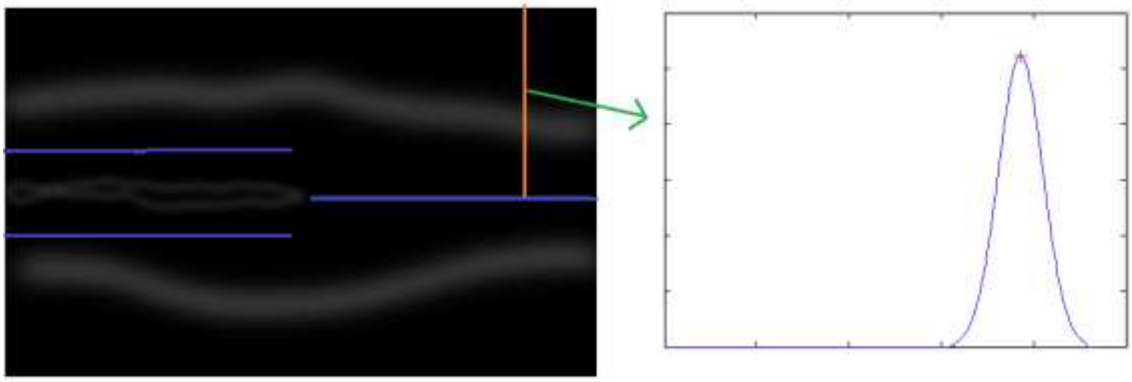

Figure 45– The orange line symbolizes the row of that length on the upper portion, and on the right side is plotted its intensity profile(the red cross is the highest point on that run and consequently, the pixel that represents that lumen boundary)

This process is used because it improves the segmentation process in two ways. Firstly, it removes the importance of the segments that are more distinct than the median, which are supposed to be noise errors, and secondly it smoothes the results giving a more natural and suitable form to the detected lumen limits. The boundaries detection applied to the original image it is displayed on figure 47.

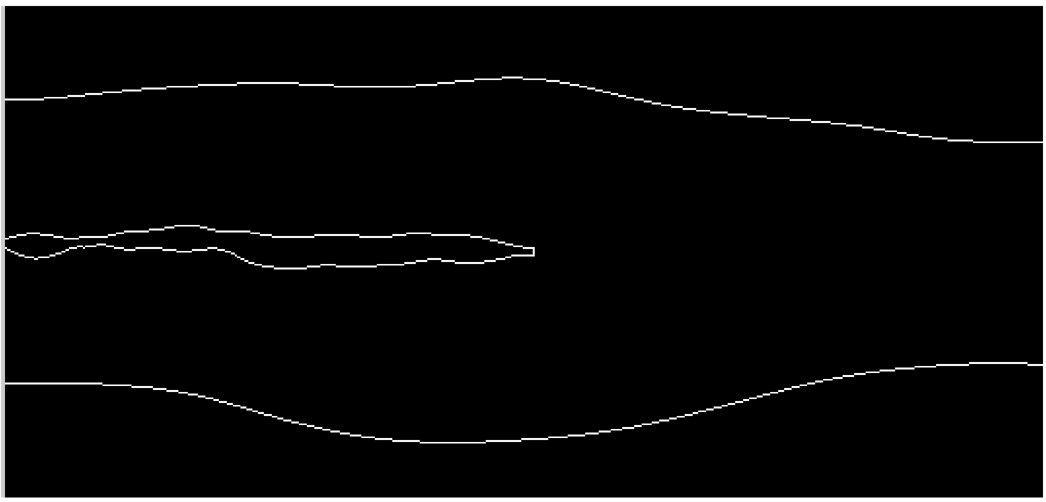

Figure 46– Final smoothed result of lumen boundaries

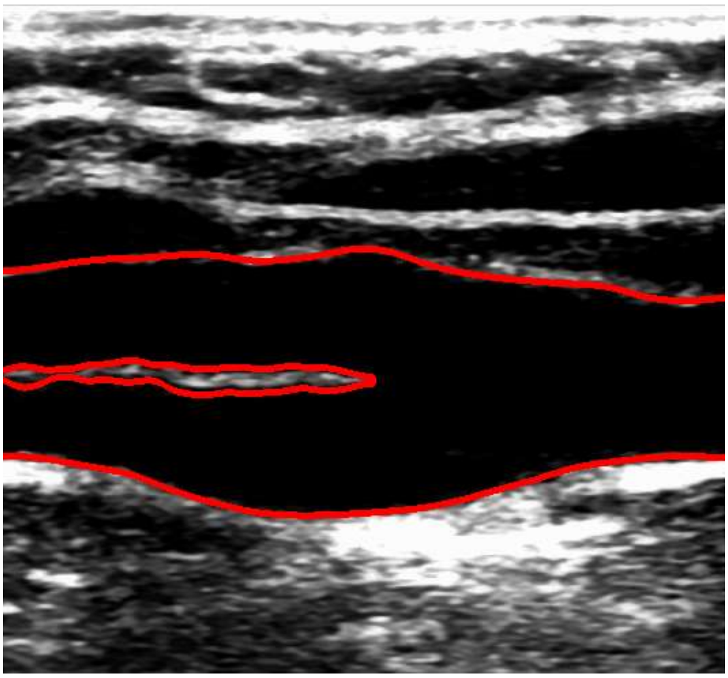

Figure 47– Lumen boundaries detected applied to the original image

5.4 3D Modeling

The lumen is commonly a cylindrical shape object. Based on that single measurement of the distance between the complementary boundaries, row by row, its segmentation can be represented on a 3D disposal. This is possible because it can be assumed that distance is actually the diameter of the lumen. Using this diameter the lumen can be represented in that row by a 3D circle, centered on the middle of the complementary boundaries. Connecting successive 3D circles, leads to a cylindrical shape creation, therefore, connecting all the circles gives us the 3D representation of the segmented lumen.

Using all the rows to compute its 3D representation requires a high computational time and it is unnecessary, so an under sampling approach is used to improve this step. This approach basically divides the lumen into a certain number of samples (figure 48), and computes their diameters. By using those diameters and connecting those samples the final 3D representation of the carotid lumen is shown in figure 49.

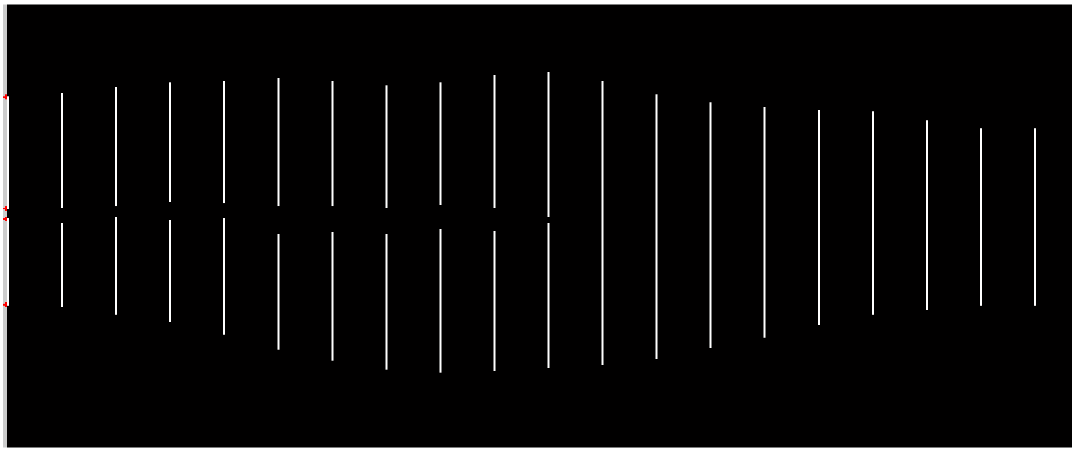

Figure 48–Lumen boundaries undersampling and computed diameter between the complementary boundaries

Figure 49– Example of a 3D representation of the lumen area, based on the method proposed

5.5 Conclusions

This chapter introduced the novel segmentation method for the carotid lumen in B-mode images. It explains detailed each step taken to achieve the segmentation and 3D representation goals.

Firstly, it shows the type of images and the pre-processing process used in this work, which is the anisotropic diffusion. Then, it travels straightly trough the algorithm itself.

The lumen inner points are a critical step of the algorithm as all the rest of the detection depends on the accuracy of these pixels, which are going to be considered the seed points.

Having those points detected, the method uses a multi scale approach to detect the lumen boundaries. This detection is based on several vertical runs for each lumen portion until it finds what is called strong gradient points. The multi scale approach is justified due to the variation of that strength for the various portions.

In the end, it showed how a 3D representation may be obtained, using the 2D lumen segmentation.

Chapter VI – Results and discussion

Chapter VI – Results and discussion

6.1 Introduction

In this chapter are presented the results of the critical points of the method. Not even all steps of the methodology are presented as some of them are redundant on the results section, and the main goal focuses on the critical points of the segmentation and detection. It is presented some of the best and worst results performed by the algorithm, as also some of the main problems the method founds.

6.2 Dataset

The proposed method is implemented on B- mode ultrasound images of the carotid artery, obtained at the hospital de S. João in Porto.

They are a total number of 15 images with CCA areas and bifurcation areas with straight, curves and descending lumen dispositions.

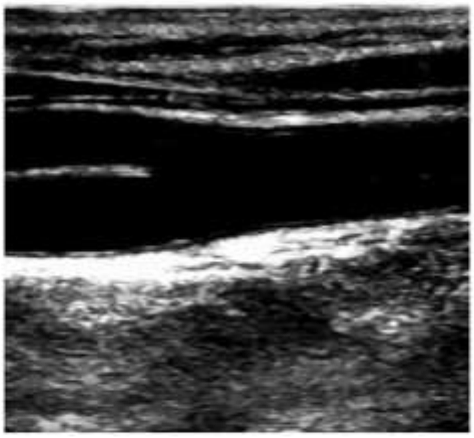

Figure 50– Example of one dataset image

6.3 Inner lumen points detection

The results of the application of the anisotropic filter combined with the closing morphological operation are shown on figure 51.

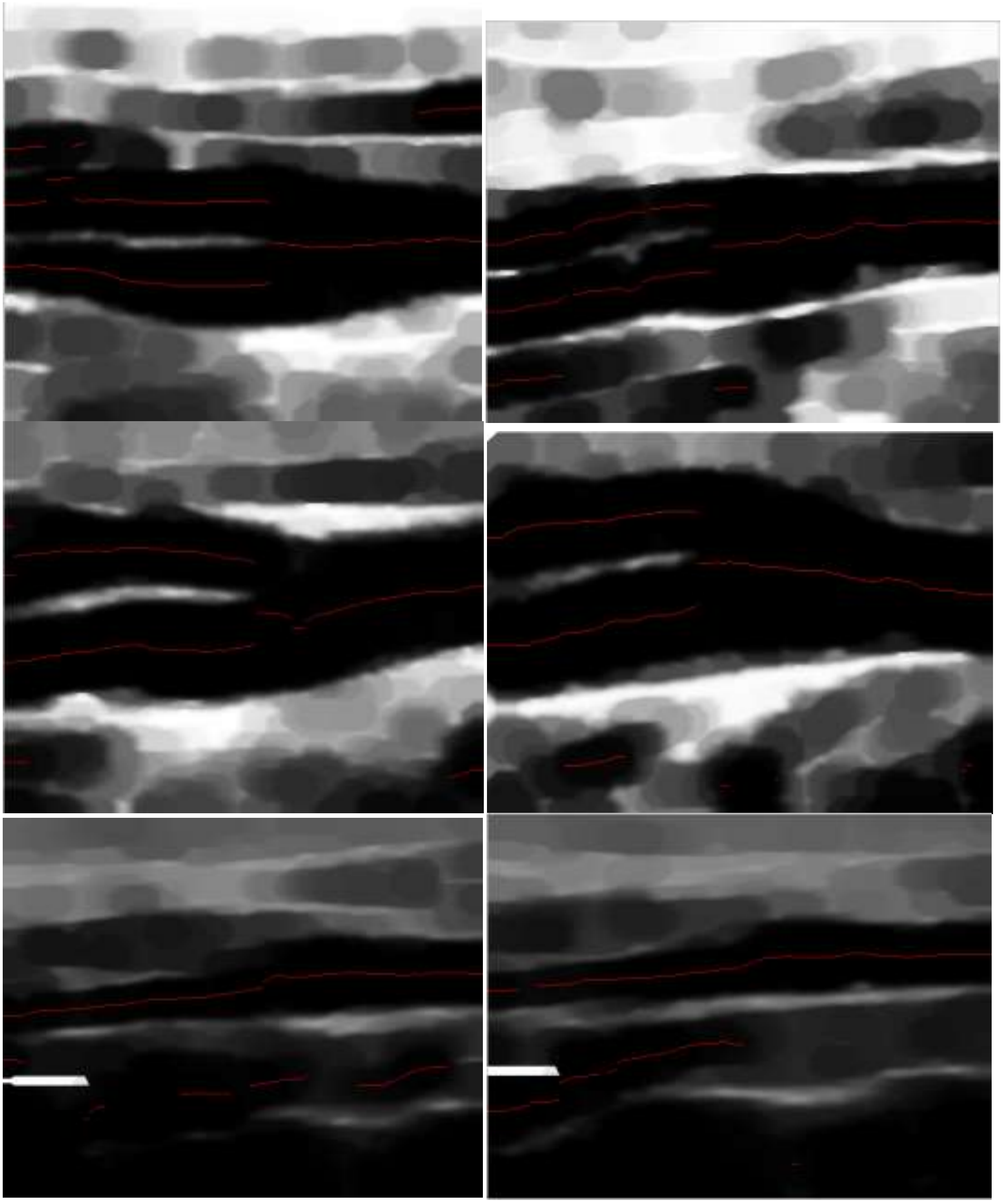

Figure 51 - Examples of the resultant lumen inner point candidates created by the combination of the anisotropic diffusion and morphological operations

It is visible that this combination allows the identification of several segments of lumen inner points on variable images. Although many false candidates were detected, this was an expected fact, due to the characteristically high noise presence and low contrast of ultrasound Imaging. Note that this method ignored all the extreme hypoechogenic zones, as it only accepts zones that have both beginning and ending point of hypoechogenic pixels.

The main goal of the ROI is to focus the algorithm processing on the significant data area, by ignoring all the other information outside of that ranged area. In other words, the goal is to successfully include on this area the lumen inner segments previously detected and ignore a good number of false candidates. The typical results and problems of this step are shown on figure 52.

Figure 52 – Examples of binary results of ROI building based on the CCA brunch

It is visible that this process is a valuable tool on false candidate removing, as it highly ignores the majority of the erroneous detected data. The search for the pixel a to build up the ROI was achieved and every image kept the most important information, the real inner lumen points; however, it is also visible that some problems still remain on the images, like gaps between segments or small false candidates.

The results of the correction and selection methods implemented on the algorithm are shown on figure 53.

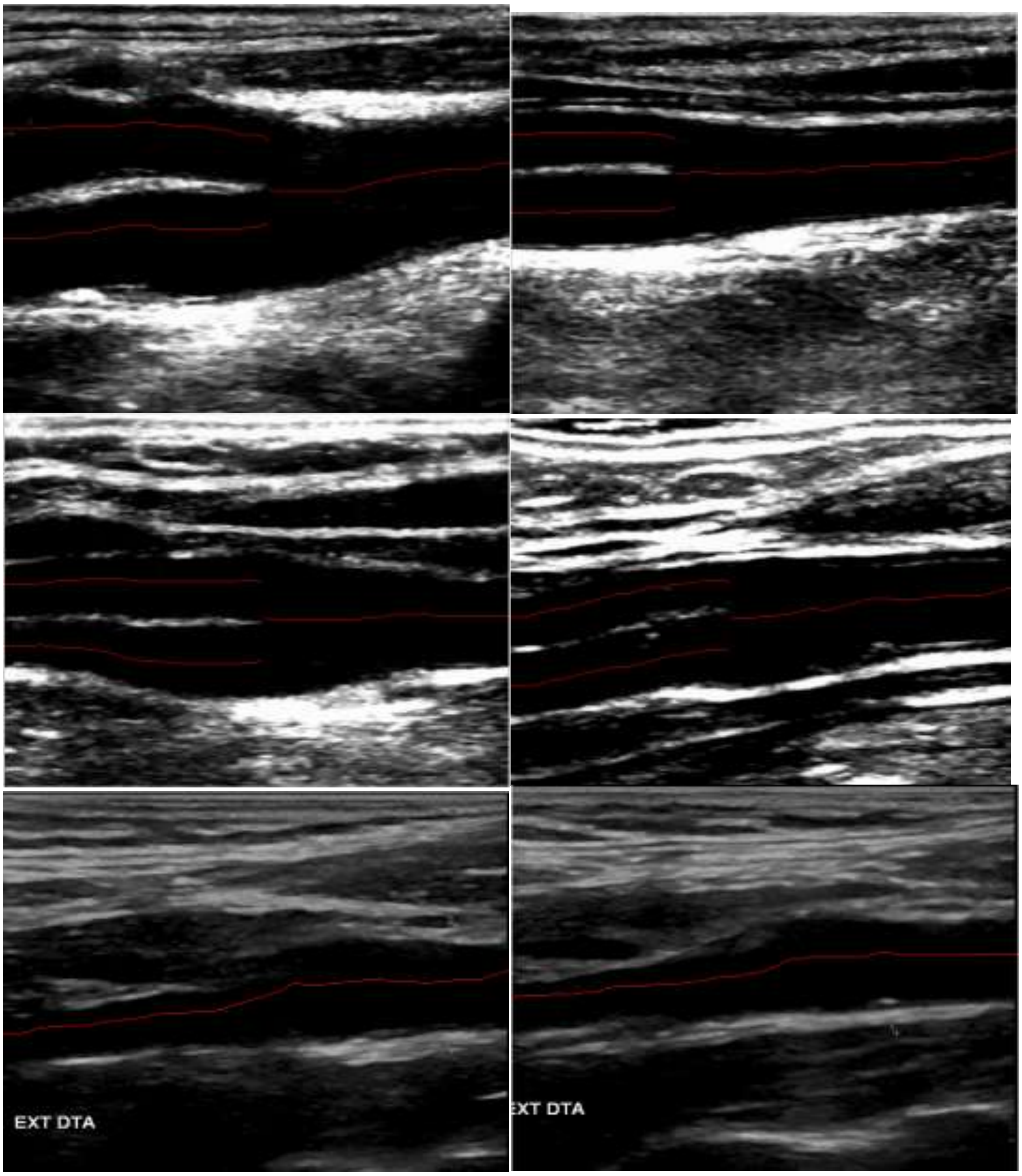

Figure 53 – Examples of results of the final inner lumen points detection

At this stage, no errors were found and all the lumen inner points row by row were found for each portion of each image. All gaps and false candidates were removed successfully.

6.4 Lumen boundaries detection

Using the detected inner lumen pixels and using it as seed points to search the lumen boundaries produced results shown in figure 54. The typical problems found in this step are also present on the images.

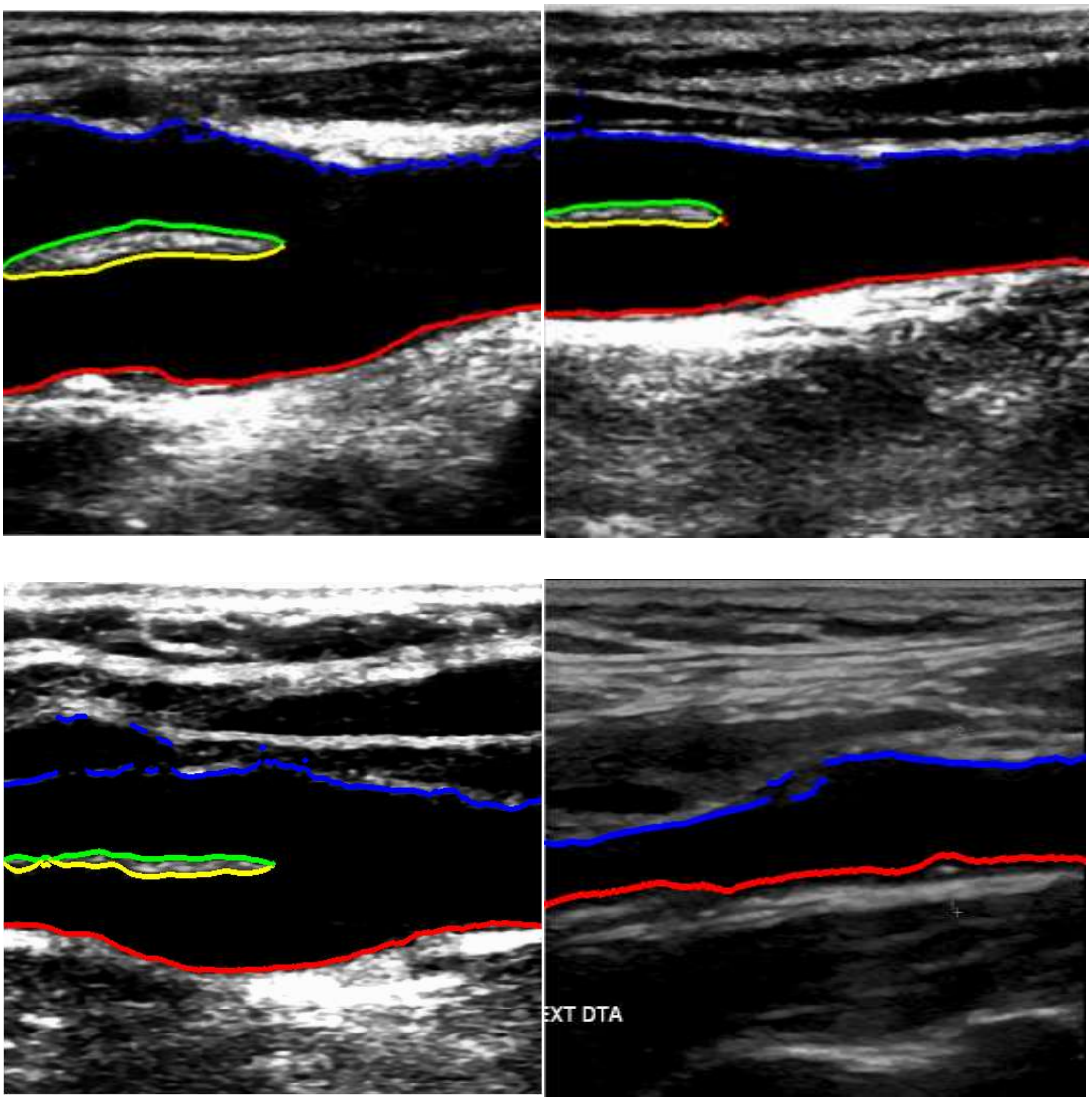

Figure 54– Examples of boundaries detection, based on the multi-scale detector

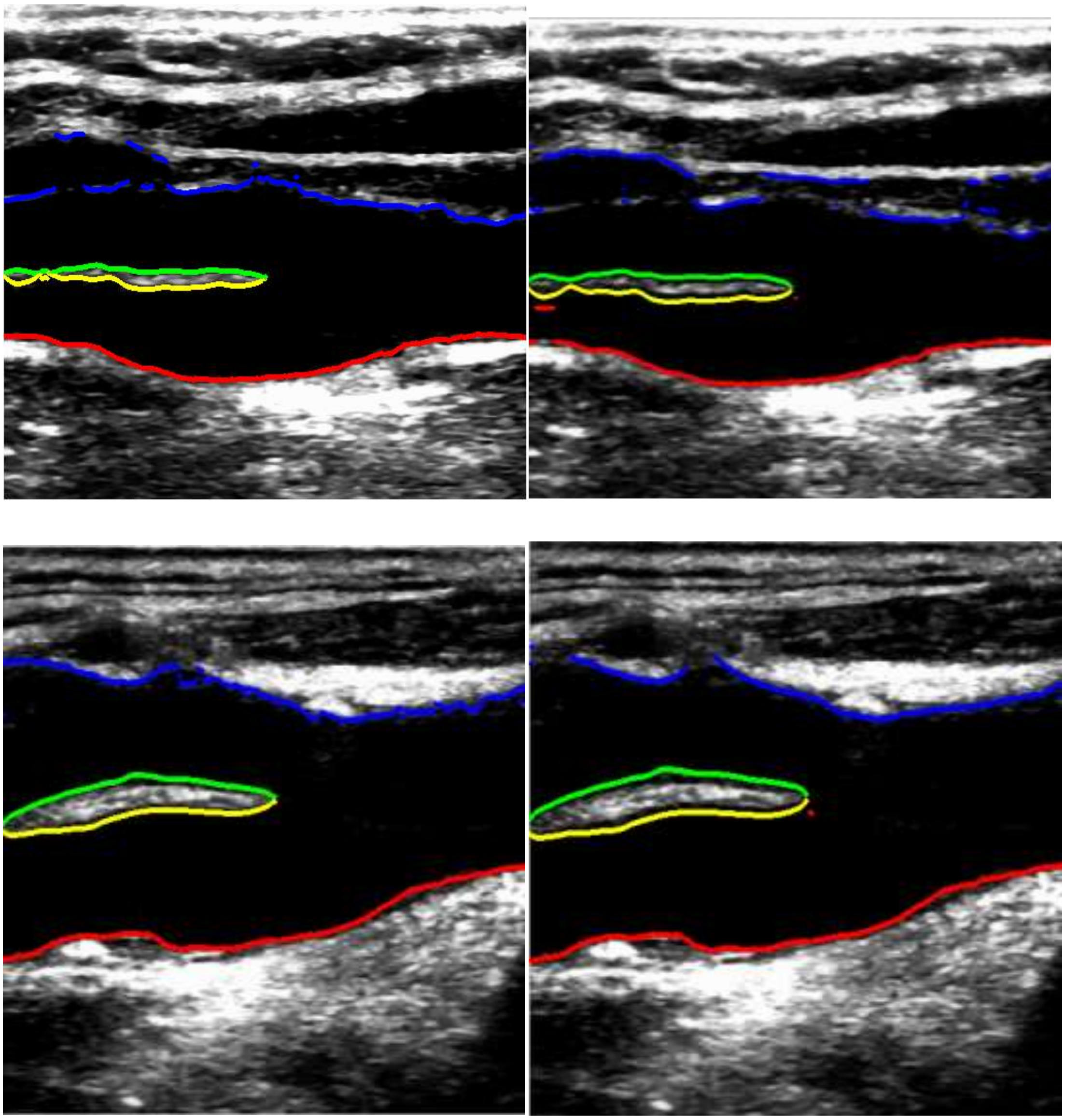

Figure 55– Difference between the multi scale detector and a single sigma application: on the left side we have the results of the multi scale and on the right the results of a single sigma

As we can see in figure 54 the majority of the detected points and segments of this method is a match to most of the lumen boundaries. Although it also detects some common errors, like gaps between segments or false detected points, this gives us a ground base to start improving the segmentation, and supports the use of smoothing in order to achieve this goal.

Note on figure 55 the difference between the detection based on the novel multi scale method and the single sigma approach. The upper portion of the lumen I highly damaged on the second case, and it may induce much more errors on the future steps.

The results of the application of this smoothing to the detected points are shown in figure 56.

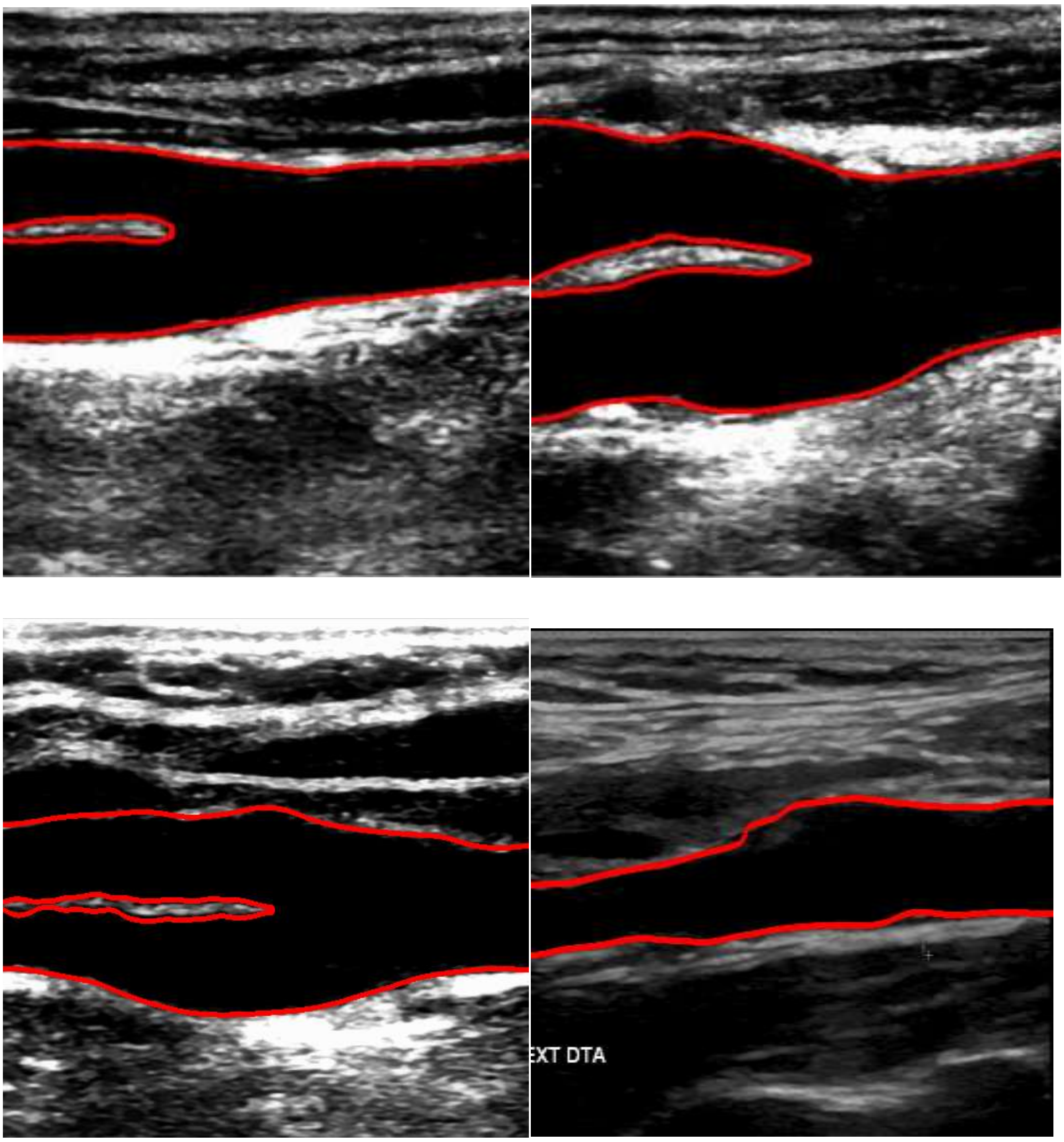

Figure 56– Final results of the lumen boundaries detection applied to the original images

The results presented above are some of the best of them obtained by using this method. There is no ground truth elaborated for a specialist in order to compare the results data, so this discussion is only based on the obvious disposal of the lumen area.

Not even all of the images obtained so perfect results like the ones above. On figure 57 it is visible some less accurate segmentations.

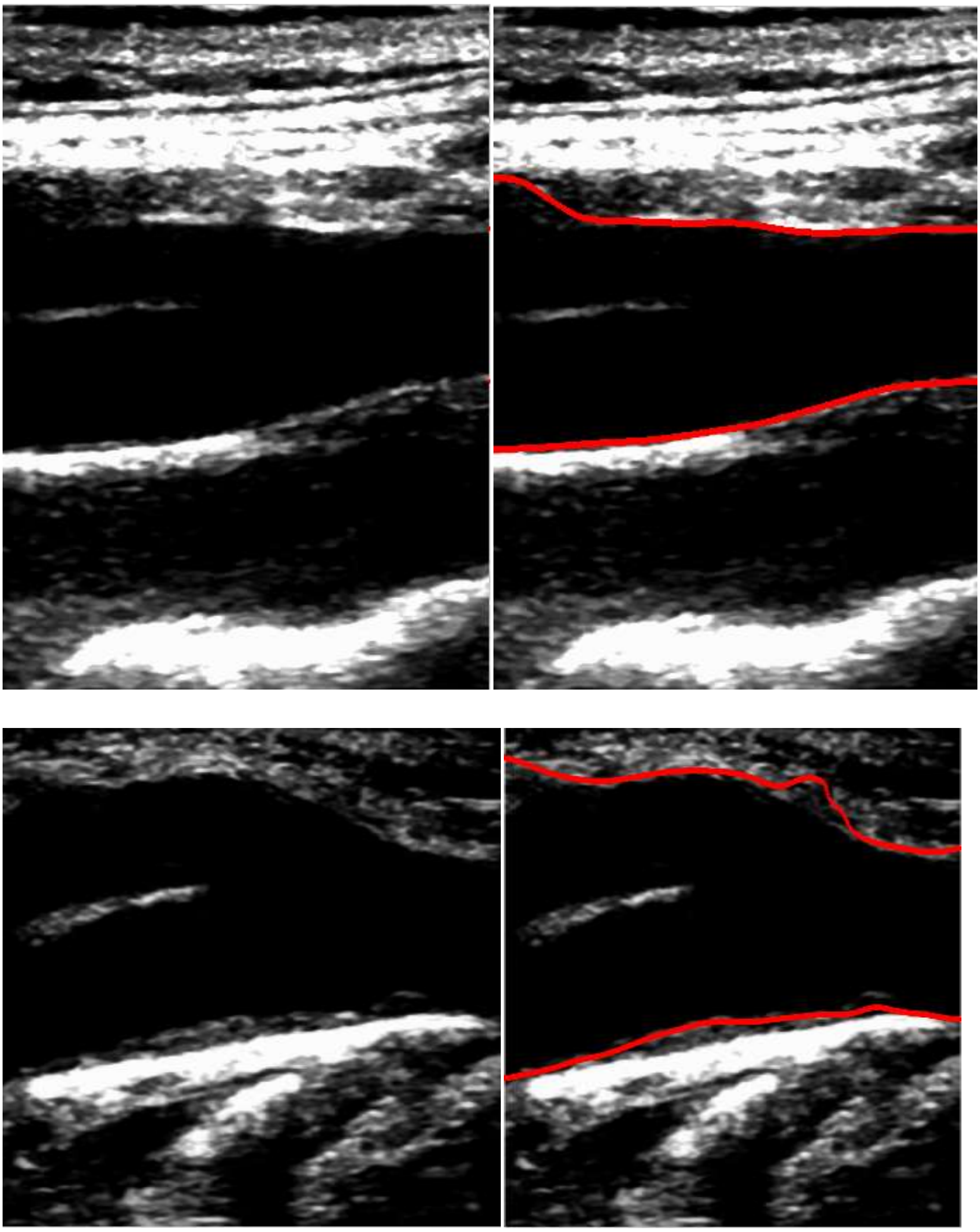

Figure 57– Some examples of segmentation errors (on the left are presented the original images)

On the first image of figure 57 the error is located on the left side of the image, where the shape of the upper portion boundary should be almost straight in their way around; however, there is presented a slight hill on it. This error is almost impossible to avoid due to the lack of definition of that boundary on the original image. As it is visible that area of the original image is completely absent of any kind of trace of the boundary.

On the second case, the boundary is visible, but it is far less powerless than the surrounding pixels leading the algorithm to slight penetrate that location.

6.5 3D Modeling

Some of the under sampling and 3D representation results are presented on figures 58, 59, 60 and 61.

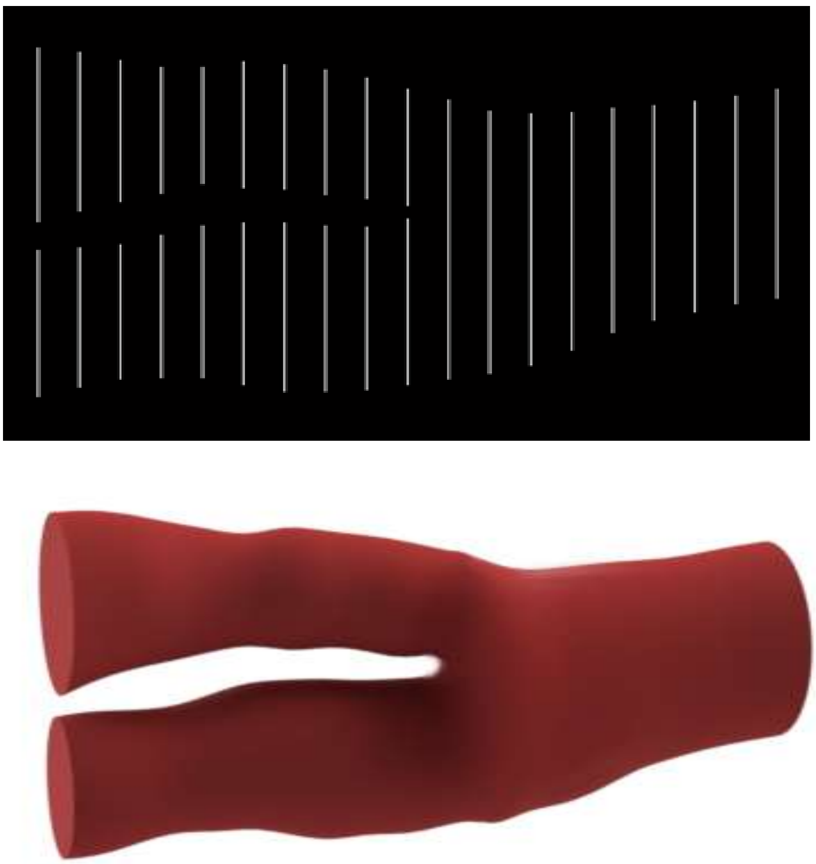

Figure 58– Example of under sampling and its 3D representation

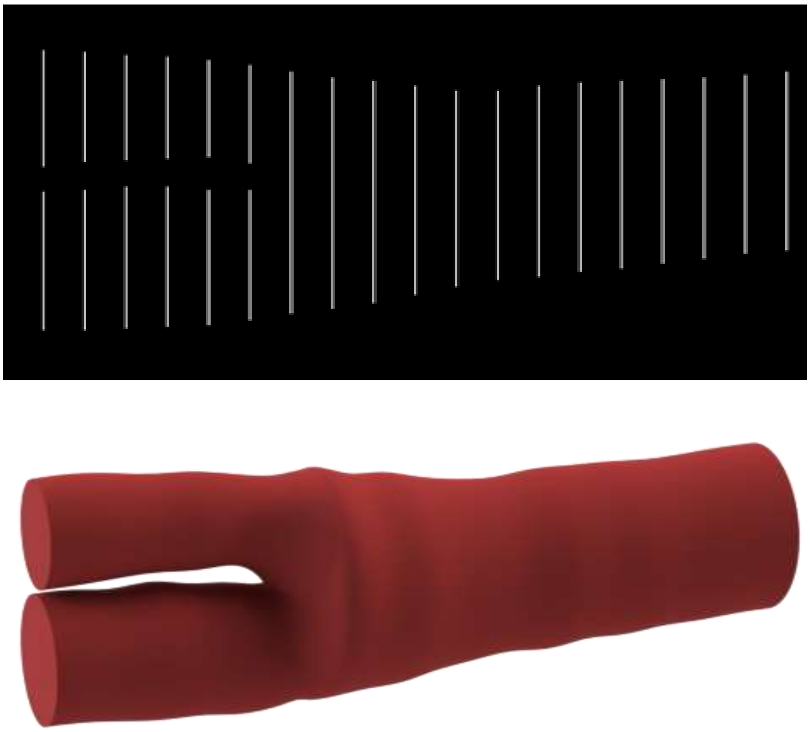

Figure 59 –Example of under sampling and its 3D representation

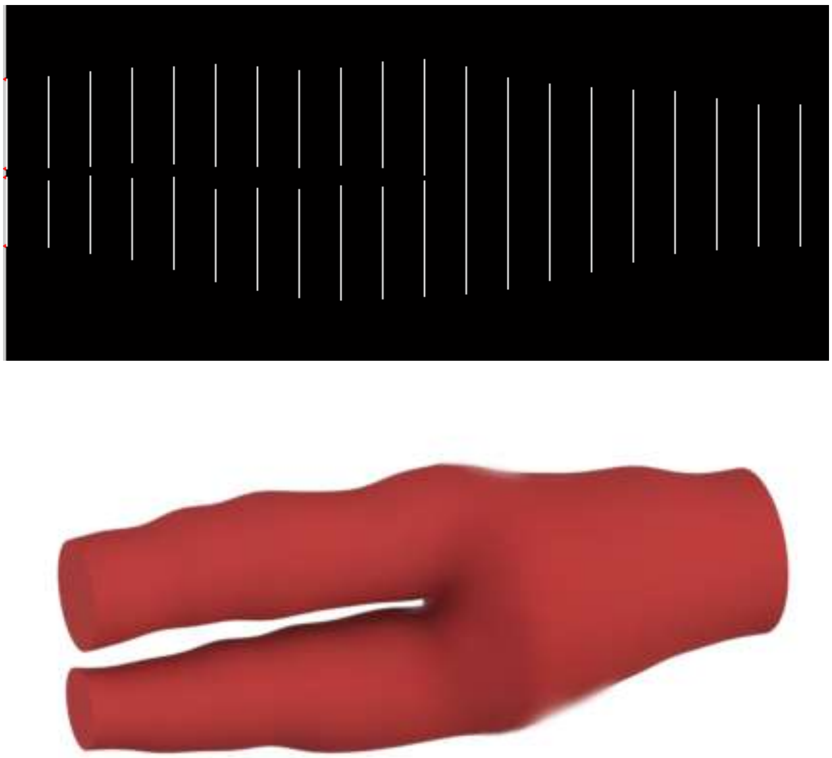

Figure 60– Example of under sampling and its 3D representation

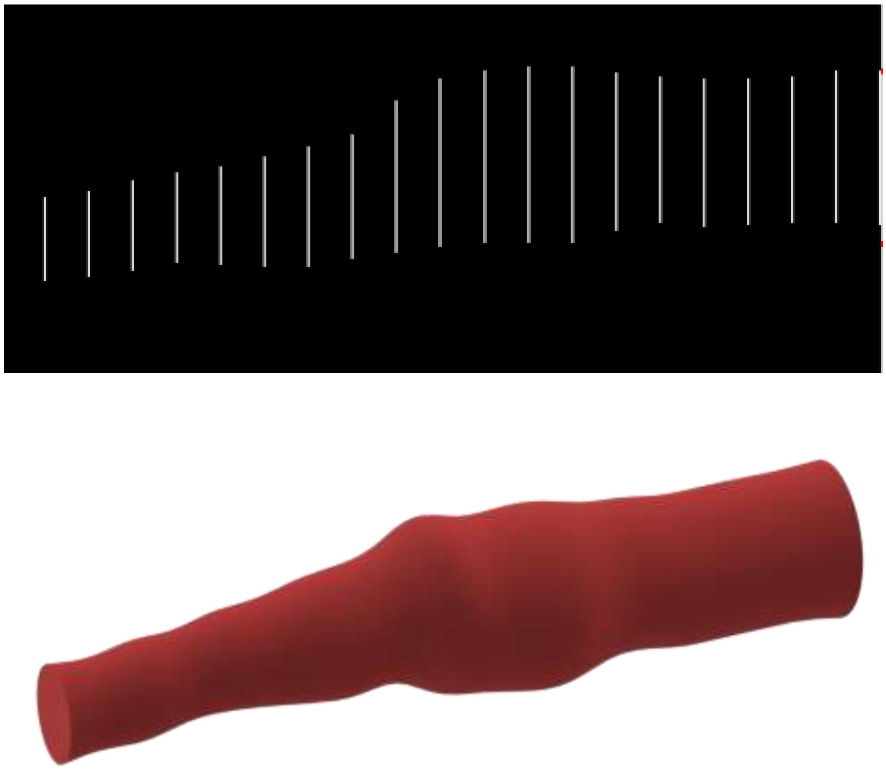

Figure 61–Example of under sampling and its 3D representation

The under sampling process showed good accuracy on being the base to represent the form of the segmented boundaries. It reduced the computational time and aided the 3D representation process to present accurate results.

Chapter VII – Conclusion and Future Remarks

Chapter VII – Conclusions and Future Remarks

Although It was impossible to evaluate the results, using the reference of one medical expert on this type of images, it can be said the results presented were highly promising, for several reasons.

As it is expected the ultrasound imaging is very difficult to process, due to the high contamination of speckle noising and low contrast; however, those difficulties were generally successfully overcome.

The inner lumen points detection is a critical step on the path the boundaries segmentation, as they work as seed points. If, for some reason, those points are not found, all the process of segmenting may be compromised. In this method, all images were successfully computed and for all of pixels row by row that defines those inner points were found, despite their noise or spatial disposal. This proves the robustness of this method on finding lumen inner points no matter what orientation the lumen area has. It also proved to be trustful on distinguishing bifurcation areas with common areas. Especially the bifurcation is one of the most troubled issues on the carotid ultrasound processing.

On the boundaries detection it is visible that the method presented quite promising results, having several good segmentation results. Although some of the images encountered some deviations from the expected ground truth, the application of a novel adaptive multi-scale segmentation method to the different portions of the lumen proved to be a successful implementation, especially compared to the single sigma approach. Some of those deviations cannot be solved due to the absent of the boundaries on the original image and lack of reference where they should develop; however, in other cases an improvement of the multi scale sensitive parameters or the creation of an even adaptive method may help to improve the removal of those errors.

The under sampling process showed to be very trustful on their task to represent the segmented boundaries with lower computation cost. It was also proven that a successful 3D representation may be implemented based on the connection of successive 3D circle projections of the diameter of the successive samples, creating the final lumen 3D shape; however, this process can also be improved, by instead of a circle projection, we use some polynomial representative of the transversal segmentation of those same carotid images. As no transversal images of the carotid were inserted on the dataset, that step could not be tested, but the idea is still up as a future work task.

On the overall, the new method showed very promising results and it is suitable to continue working on; however, a higher number of dataset images should be added in order to take the final conclusion of it.

References

BOVIK, A.L. (2009); The essential Guide to image Processing. Elsevier.ISBN:9780123744579

CHENG, D.C.; Schmidt-Trucksass, A.; Cheng, K.S.; Burkhardt, H. (2002); Using snakes to detect the intimal and adventitial layers of the common carotid artery wall in sonographic images, Comput. Methods Prog. Biomed. 67 (1) 27–37.

DELSANTO; Molinari, F.; Giustetto, P.; Liboni, W.; Badalamenti, S.; Suri, J.S. (2007); Characterization of a completely user-independent algorithm for carotid artery segmentation in 2D ultrasound images, IEEE Trans. Instrum. Meas. 56 (4) (2007) 1265–1274.

DELSANTO; Molinari, F.; Giustetto, P.; Liboni, W. ;Badalamenti, S. (2007); CULEX-completely user-independent layers extraction: ultrasonic carotid artery images segmentation, Conf. Proc. IEEE Eng. Med. Biol. Soc. 6 (2005) 6468–6471.

LOIZOU, C.P.; Pattichis, C.S.; Pantziaris, M.; Tyllis, T.; Nicolaides, A.; Snakes based segmentation of the common carotid artery intima media, Med. Biol. Eng. Comput. 45 (1) 35–49.

DESTREMPES, F. ; Meunier, J. ; Giroux, M.F. ; Soulez, G. ; Cloutier, G. (2009); Segmentation in ultrasonic B-mode images of healthy carotid arteries using mixtures of Nakagami distributions and stochastic optimization, IEEE Trans. Med. Imaging 28 (2) 215–229.

DRAKE, Richard L.; Vogl Wayne; Mitchell, Adam W.M. (2004) ; Gray's Anatomy for Students. Churchill Living stone. Elsevier Health Sciences. ISBN 13:9780443066122

DOUGHERTY, Geoff (2009); Digital Image Processing for Medical Applications. Cambridge University PRESS.ISBN:9780511533433

FATIA, F. ; Gemignani, V. ; Bianchini, E. ; Giannarelli, C. ; Ghiadoni, L.; Demi, M. (2008); Real-time measurement system for evaluation of the carotid intima-media thickness with a robust edge operator, J. Ultrasound Med. 27 (9) 1353–1361.

GOLEMATI, S. ; Stoitsis, J. ; Sifakis, E.G. ; Balkizas, T. ; Nikita, K.S. (2007); Using the Hough transform to segment ultrasound images of longitudinal and transverse sections of the carotid artery, Ultrasound Med. Biol. 33 (12) 1918–1932. [82]

GONZALEZ, Rafael C.; Woods, Richard E. (2001); Digital image Processing; 2nd Edition; Prentice Hall. ISBN: 0201180758

GUTIERREZ, M.A.; Pilon, S.G. Lage, P.E.; Kopel, L. ; Carvalho, R.T. S.S. Furuie, (2002); Automatic measurement of carotid diameter and wall thickness in ultrasound images, Comput. Cardiol. 29 359–362.

LIANG, Q.; Wendelhag, I. ; Wikstrand, J. ; Gustavsson, T. (2000); A multiscale dynamic programming procedure for boundary detection in ultrasonic artery images, IEEE Trans. Med. Imaging 19 (2) 127–142.

LIGUORI, C.; Paolillo, A.; Pietrosanto, A. (2001); An automatic measurement system for the evaluation of carotid intima-media thickness, IEEE Trans. Instrum. Meas. 50 (6) 1684–1691.

PRINCE, J.L.; Links, J.M. (2005); Medical Imaging: Signals and Systems. Prentice Hall. ISBN-13: 978-0130653536

MAURITS, N.M.; Loots, G.E (2007); The influence of vessel wall elasticity and peripheral resistance on the carotid artery flow wave form: A CFD model compare to in vivo ultrasound measurements; J. Biomech. 40 (2007) 427-436.

MOLINARI, F.; Delsanto, S.; Giustetto, P . ; W. Liboni, W. ; Badalamenti, S.; J.S. Suri; User-independent Plaque Segmentation and Accurate Intima-media Thickness Measurement of Carotid Artery Wall Using Ultrasound, Artech House, Norwood, MA, 2008, pp. 111–140.

MOLINARI F. ; Zeng, G.; Suri, J.S. (2010) ; A state of the art review on intima-media thickness (IMT) measurement and wall segmentation techniques for carotid ultrasound.: Elsevier

MOLINARI, F. ;Zeng, G. ; Suri, J.S. (2010); An integrated approach to computer-based automated tracing and its validation for 200 common carotid arterial wall ultrasound images: a new technique, J. Ultrasound Med. 29 399–418.

MOORE, Keith L.; Dalley, Arthur F. (2006); Clinically Oriented Anatomy ; 5th Edition; Lippincott Williams & Wilkins. ISBN 13:9780781736398

NETTER, F. H. (2002); Atlas of Human Anatomy; 3rd Edition; Saunders. ISBN-10: 1929007116

ROCHA, Rui (2010); Segmentation of the Carotid Artery in Ultrasound Images. Biomedical Image Analysis.Master Degree on Biongineering.

RANGAYYAN, Rangaraj M. (2005) – Biomedical Image Analysis. CRC PRESS.ISBN:0849396956

RUSS, John C. (2007); The image processing handbook, 5th Edition, Taylor and Francis group. ISBN: 0849372542

SALADIN, Kenneth S. (2003); Anatomy & Physiology: The Unity of Form and Function. 3th Edition. ISBN: 0072919264

SEELEY, Rod R.; Stephens, Trent D.; Tate, Philip (2004); Anatomia e Fisiologia; 6º edição.; Loures: Lusociência – EdiçõesTécnicas e Científicas, Lda. ISBN 972-8930-07-0

STEIN, J.H. ; Korcarz, C.E. ; Mays, M.E. ; Douglas, P.S. ; Palta, M. ; Zhang, H.; Lecaire, T. (2005) ; Asemiautomated ultrasound border detection program that facilitates clinical measurement of ultrasound carotid intima-media thickness, J. Am. Soc. Echocardiogr. 18 (3) 244–251.

TOUBOUL, P.J. ; Prati, P. ; Scarabin, P.Y. ; Adrai, E.; Ducimetiere, Thibout, P. (1992); Use of monitoring software to improve the measurement of carotid wall thickness by B-mode imaging, J. Hypertens. 10 (Suppl. 5) S37–41.

WENDELHAG, Liang, Q.; Gustavsson; Wikstrand, J. (1997); A new automated computerized analyzing system simplifies readings and reduces the variability in ultrasound measurement of intima-media thickness, Stroke 28 (11) 2195–2200.

WILLIANS, D.J.; Shah, M. (1992) ; A fast algorithm for active contours and curvature estimation, CVGIP-Image Understand. 55 (1) 14–26.